



Published in final edited form as:

Cell Rep. 2021 November 23; 37(8): 110040. doi:10.1016/j.celrep.2021.110040.

Redox-sensitive CDC-42 clustering promotes wound closure in *C. elegans*

Jingxiu Xu^{1,7}, Xinan Meng^{1,2,7}, Qingxian Yang¹, Jianqin Zhang³, Wei Hu⁴, Hongying Fu¹, Jack Wei Chen⁴, Weirui Ma⁵, Andrew D. Chisholm⁶, Qiming Sun³, Suhong Xu^{1,2,8,*}

¹Center for Stem Cell and Regenerative Medicine and Department of Cardiology of the Second Affiliated Hospital, Zhejiang University School of Medicine, Hangzhou 310058, China

²Zhejiang University-University of Edinburgh Institute, Key Laboratory of Tissue Engineering and Regenerative Medicine of Zhejiang Province, Zhejiang University School of Medicine, Hangzhou 310058, China

³Department of Biochemistry and Department of Cardiology of the Second Affiliated Hospital, Zhejiang University School of Medicine, Hangzhou 310058, China

⁴Department of Cell Biology and Department of Cardiology of the Second Affiliated Hospital, Zhejiang University School of Medicine, Hangzhou 310058, China

⁵Life Sciences Institute, Zhejiang University, Hangzhou 310058, China

⁶Division of Biological Sciences, Section of Cell and Developmental Biology, University of California, San Diego, 9500 Gilman Drive, La Jolla, CA 92093, USA

⁷These authors contributed equally

⁸Lead contact

SUMMARY

Tissue damage induces immediate-early signals, activating Rho small GTPases to trigger actin polymerization essential for later wound repair. However, how tissue damage is sensed to activate Rho small GTPases locally remains elusive. Here, we found that wounding the *C. elegans* epidermis induces rapid relocalization of CDC-42 into plasma membrane-associated clusters, which subsequently recruits WASP/WSP-1 to trigger actin polymerization to close the wound. In addition, wounding induces a local transient increase and subsequent reduction of H₂O₂, which negatively regulates the clustering of CDC-42 and wound closure. CDC-42 CAAX motif-mediated prenylation and polybasic region-mediated cation-phospholipid interaction are both required for

*Correspondence: shxu@zju.edu.cn.

AUTHOR CONTRIBUTIONS

S.X. conceived the study and designed experiments. J.X. designed and performed most of the experiments. X.M. designed and generated most transgenic animals and interpreted the data. J.X. performed protein purification and biochemical experiments. Q.Y. and H.F. made constructs and performed the wounding assay. J.W.C., W.M., and Q.S. supervised the biochemical experiments. S.X., A.D.C., J.X., and X.M. wrote the manuscript.

SUPPLEMENTAL INFORMATION

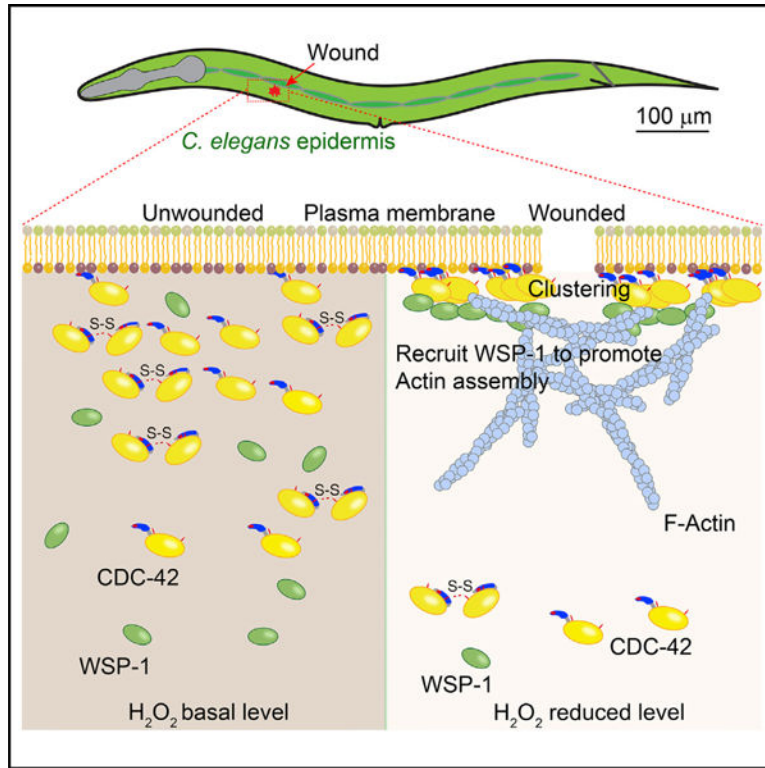
Supplemental information can be found online at <https://doi.org/10.1016/j.celrep.2021.110040>.

DECLARATION OF INTERESTS

The authors declare no competing interests.

its clustering. Cysteine residues participate in intermolecular disulfide bonds to reduce membrane association and are required for negative regulation of CDC-42 clustering by H₂O₂. Collectively, our findings suggest that H₂O₂-regulated fine-tuning of CDC-42 localization can create a distinct biomolecular cluster that facilitates rapid epithelial wound repair after injury.

Graphical abstract



In brief

Tissues must immediately detect and respond to injury before repairing the damage. Here, Xu et al. report that wounding induced a local increase and subsequent reduction of H₂O₂. This regulates fine-tuning of CDC-42 clustering to recruit WSP-1 and promote actin polymerization-based wound closure in *C. elegans* epidermis.

INTRODUCTION

The epidermis in all animals acts as a physical barrier preventing damage caused by mechanical injury and external pathogens (Eming et al., 2017; Mosteiro et al., 2016). The ability to efficiently heal wounds and maintain epidermal integrity is essential for animal survival. Mechanical damage acts via interrelated biochemical pathways to convert physical cues to biological responses and plays critical roles in regulating tissue repair and regeneration in various organisms (Gurtner et al., 2008; Wong et al., 2012). The force generated in these biological processes relies on the interaction between actin filaments and myosin motors. A contractile actomyosin ring assembles within seconds to

minutes upon wounding (Martin and Lewis, 1992) and is dependent on Ca^{2+} -activated Rho family guanosine triphosphatases (GTPases) or actin filament-severing proteins (Benink and Bement, 2005; Burkel et al., 2012; Wood et al., 2002).

Actin assembles around the wound as a supra-cellular cable that rapidly contracts to close the wound hole, a feature of epithelial wound closure conserved from invertebrates to vertebrates (Clark et al., 2009; Sonnemann and Bement, 2011). In the cellular environment, actin filaments are assembled with the assistance of the actin nucleator Arp2/3 complex, creating branched filaments upon activation of CDC-42 (Burkel et al., 2012). The CDC-42 Rho family GTPase plays a conserved role in regulating actin polymerization and filopodium formation in metazoans (Burkel et al., 2012) and is essential for actin-based wound closure in *C. elegans* (Xu and Chisholm, 2011). Notably, the nucleation-promoting factor neural Wiskott-Aldrich syndrome protein (N-WASP) is able to trigger actin polymerization through multivalent interaction mediated phase separation and the activation of Arp2/3 (Banjade and Rosen, 2014; Li et al., 2012). However, much less is known about how tissues sense mechanical injury to influence these kinds of relocalization or phase changes and regulate actin remodeling.

Rapid responses to cell or tissue wounding are critical for subsequent healing and animal survival (Niethammer, 2016). Tissue damage induces transcription-independent signals involving Ca^{2+} and H_2O_2 , which promote wound repair and inflammatory cell migration (Cordeiro and Jacinto, 2013). To stimulate immune cell chemotaxis, H_2O_2 promotes the modification of a thiol switch in the tyrosine kinase LYN (Yoo et al., 2011), the transcription of chemokines (de Oliveira et al., 2014, 2015; Martínez-Navarro et al., 2020), and wound repair and regenerative events in numerous organisms (Cordeiro and Jacinto, 2013; Suzuki and Mittler, 2012). Reactive oxygen species (ROS) have also recently been implicated in playing important roles in regulating actin and myosin accumulation at the wound site (Hunter et al., 2018; Ponte et al., 2020; Xu and Chisholm, 2014a). However, the precise biochemical mechanisms by which H_2O_2 regulates this rapid action are not fully known, as the biological effects of H_2O_2 are not mediated by classical receptor-ligand interactions but by its ability to oxidize susceptible molecular targets.

Here, using *C. elegans* as a model, we studied how wound response and repair are sensed and initiated in the syncytial epidermis. We show that epidermal wounding induces a rapid membrane-associated cluster formation of CDC-42, which subsequently recruits WSP-1 to initiate local actin polymerization. In addition, we find that wounding induces a transient and local increase in H_2O_2 signal, followed by a more prolonged decrease in H_2O_2 , which enables temporal fine-tuning of the CDC-42 clustering *in vivo*. Furthermore, we show that CDC-42 residues cysteine (Cys) 18 and 105, which can participate in disulfide bond formation, are required for the negative regulation of CDC-42 by H_2O_2 . Our findings suggest that wounding-induced H_2O_2 regulates CDC-42 to create a distinct membrane-associated signaling platform to facilitate actin-based epidermal wound closure *in vivo*.

RESULTS

Wounding triggers rapid clustering of CDC-42 in *C. elegans* syncytial epidermis

To assess the molecular dynamics and rapid activation of CDC-42 protein, we expressed a GFP fusion CDC-42 specifically in the epidermis and performed time-lapse confocal imaging before and after wounding (Figure S1A). GFP::CDC-42 fluorescence was punctate and partially colocalized with the plasma membrane (Figure S1A; Video S1 with the Mendeley dataset: 10.17632/zy2gmmcxp8.1). Prior to wounding, submicrometer-sized GFP::CDC-42 puncta were small and dim (Figure S1A). After needle wounding, we detected numerous larger bright GFP::CDC-42 puncta formed within 5 min at the wound site (Figures S1A and S1B). In addition, the size and number of the wounding-induced GFP::CDC-42 puncta correlated with the expression level of CDC-42 (Figures S1C–S1E).

To examine CDC-42 puncta formation with the higher temporal resolution, we imaged GFP::CDC-42 dynamics before and after wounding using MicroPoint UV laser and spinning disk confocal microscope (Figure 1A). Upon wounding, numerous micrometer-sized CDC-42 puncta formed within 10 s (Figures 1A and 1B; Video S2 with the Mendeley dataset: 10.17632/zy2gmmcxp8.1) and gradually grew in size and fluorescence intensity at the wound region (Figures 1C and 1D; Video S3 with the Mendeley dataset: 10.17632/zy2gmmcxp8.1). Analysis of these puncta showed that small GFP::CDC-42 puncta fused into larger ones near the wound site (Figure 1E; Video S4 with the Mendeley dataset: 10.17632/zy2gmmcxp8.1), and large GFP::CDC-42 puncta underwent fission into smaller structures (Figure 1F; Video S5 with the Mendeley dataset: 10.17632/zy2gmmcxp8.1). GFP::CDC-42 puncta formed close to the wound site and up to 50 μm around the wounds (Figure S1F), with numerous puncta colocalized with the plasma membrane marker *myr::mKate2* (Figure S1F; Videos S6 and S7) and phosphatidylinositol biphosphate PIP2 (GFP fused with PH domain from rat PLC- δ 1) (Figure S1G; Video S8 with the Mendeley dataset: 10.17632/zy2gmmcxp8.1), consistent with the previous observation that activated CDC-42 interacts with PIP2 (Higgs and Pollard, 2000). As the wounding-induced puncta are larger, brighter, and colocalized with membrane components, we thus use “clustering” to describe these wounding-induced changes in GFP::CDC-42 localization.

To determine whether endogenous CDC-42 responds to wounding similarly, we performed immunostaining with anti-CDC-42 antibody and observed similar cluster formation as GFP::CDC-42 (Figure S1H). We further generated *gfp::cdc-42* knockin at the endogenous *cdc-42* locus (Figure 1G). Consistent with GFP::CDC-42 single-copy insertion and the immunostaining results, the knockin GFP::CDC-42 also formed clusters after laser wounding (Figure 1G), and the submicrometer-sized clusters gradually grew in size and fluorescence intensity (Figure 1G; Video S9 with the Mendeley dataset: 10.17632/zy2gmmcxp8.1), with similar fusion behaviors (Video S10 with the Mendeley dataset: 10.17632/zy2gmmcxp8.1). Thus, wounding induces rapid clustering of endogenous CDC-42 at the wound areas.

To further analyze the properties of CDC-42 clusters, we examined their turnover by using fluorescence recovery after photobleaching (FRAP) adjacent to the wound margin. The fluorescence intensity of GFP::CDC-42 clusters recovered by 50% within 100 s after

bleaching ($t_{1/2}$ [one-half recovered] = 100 s) (Figure 1H; Videos S11 and S12). It was notable that recovery of fluorescence was observed upon bleaching of a sub-region within a CDC-42 cluster and a whole CDC-42 punctum (Figure 1H; Figures S1I and S1J). Thus, these results suggest that CDC-42 molecules exchange into and out of the cluster from the neighbor region in the epidermal cell.

CDC-42 clusters recruit WSP-1 to promote actin polymerization-based wound closure

Given this observation that wounding triggers local clustering of CDC-42 at the wound site, we tested whether these clusters play roles in actin polymerization-based wound closure. We coexpressed the F-actin marker LifeAct::tagBFP together with GFP::CDC-42 in the epidermis and analyzed actin polymerization and CDC-42 clustering at the wound site (Figure 2A; Figure S2A). We observed that the CDC-42 clusters formed before actin was polymerized and that actin polymerization can be detected close to the CDC-42 clusters (Figure 2A; Figure S2A; Video S13 with the Mendeley dataset: 10.17632/zy2gmmcxp8.1). As CDC-42 clusters became enlarged, numerous concentrated actin rings formed at the wound site (Figure 2A; Figure S2B). RNAi knockdown of *cdc-42* completely blocked actin ring formation at wound sites (Figure S2C), suggesting that CDC-42 clustering upon wounding is required for actin ring-based wound closure.

In other contexts, CDC-42 promotes actin polymerization through the actin nucleation factor N-WASP. We therefore examined the dynamics of *C. elegans* N-WASP, WSP-1 (Sawa et al., 2003), in the epidermis before and after wounding. GFP::WSP-1 formed puncta in the adult epidermis and underwent rapid and dynamic movement (Figure S2D; Video S14 with the Mendeley dataset: 10.17632/zy2gmmcxp8.1). GFP::WSP-1 puncta accumulated at the wound site after both needle and laser wounding (Figure S2D; Videos S15 and S16). GFP::WSP-1 puncta at the wound site showed partial recovery in FRAP experiments (Figures S2E and S2F; Video S17 with the Mendeley dataset: 10.17632/zy2gmmcxp8.1), suggesting that WSP-1 in puncta may undergo slower exchange with cytosolic WSP-1.

To understand the relationship between CDC-42 clusters and WSP-1 accumulation, we coexpressed mKate2::CDC-42 with GFP::WSP-1 and observed that the GFP::WSP-1 was increasingly accumulated to the mKate2::CDC-42 clusters at the wound site a few minutes after wounding (Figures 2C and 2D; Figure S2G; Video S18 with the Mendeley dataset: 10.17632/zy2gmmcxp8.1). Moreover, small CDC-42 clusters and WSP-1 puncta tended to coalesce into large clusters (Figure 2C; Video S19 with the Mendeley dataset: 10.17632/zy2gmmcxp8.1). Finally, to test if CDC-42 might affect the recruitment of WSP-1, we knocked down *cdc-42* specifically in the epidermis by RNAi and observed a significant reduction in GFP::WSP-1 puncta number after wounding (Figures 2E and 2F). In contrast, knockdown of *wsp-1* did not affect CDC-42 clustering after wounding (Figures S2H and S2I). Together, these results suggest that wounding-induced CDC-42 clustering recruits WSP-1 to promote actin polymerization-based wound closure.

Wounding induces a local burst and reduction of H₂O₂ in the syncytial epidermis

To determine how wounding induces CDC-42 clustering on such a short timescale, we examined the early wound response signal H₂O₂, which has been shown to be critical to

wound response and regeneration in numerous multicellular organisms (Love et al., 2013; Niethammer et al., 2009; Pase et al., 2012) but was less known within the cytosol in single-cell wounding. We expressed the genetically encoded H₂O₂ sensor roGFP2::Orp1 in the epidermal cell to examine the H₂O₂ signal before and after wounding (Figure S3A). The pH-insensitive roGFP2::Orp1 is a fusion of roGFP2 to *Drosophila* oxidant receptor peroxidase 1 (Orp1) (Figure S3A), a thiol peroxidase widely used as an H₂O₂-specific and reversible sensor in numerous model organisms, including *C. elegans* (Braeckman et al., 2016; Morgan et al., 2011; Qiu et al., 2008; Ramachandran et al., 2004).

We observed a local increase of roGFP2::Orp1 signal ratio (405/488 nm) at the wound site starting 2 s after laser wounding (Figures 3A and 3B; Figures S3B and S3C; Video S20 with the Mendeley dataset: 10.17632/zy2gmmcxp8.1). roGFP2::Orp1 signal was significantly increased until it reached a peak at 5 s after wounding (Figure 3B; Figure S3C). The increased roGFP2::Orp1 signal spread from the wound site to the neighboring area within seconds (Figure 3C). The spread distance of the roGFP2::Orp1 transient burst was approximately 90 μm (Figure S3D). Strikingly, the increased roGFP-Orp1 signal then declined until below the unwounded baseline, first at the wound site and later in the adjacent region (Figure 3C; Figure S3C). roGFP2::Orp1 signal did not recover to baseline levels for at least 1 h post-wounding (h.p.w.) (Figures S3E and S3F; Video S21 with the Mendeley dataset: 10.17632/zy2gmmcxp8.1). We observed a decrease in the roGF-P2::Orp1 signal after needle wounding (Figure S3G), likely because of the delay between needle wounding and imaging in our current procedure. Thus, our observations suggest that either laser or puncture wounding triggers an initial brief increase in H₂O₂ followed by a more prolonged decrease below normal for at least 1 h.

Dual oxidase is a well-known requirement for H₂O₂ production in metazoans after injury (Suzuki and Mittler, 2012). To test whether dual oxidase is required for the H₂O₂ transient burst in the epidermal cell, we examined the roGFP2::Orp1 signal in the mutants of two nematode homologs: *duox-2* and *bli-3* (Edens et al., 2001; Meitzler et al., 2010). We did not observe an increase but rather a significant reduction of roGFP2::Orp1 signal in the *duox-2* and *bli-3* mutants after laser wounding (Figures 3D–3F; Figures S3H–S3J; Video S22 with the Mendeley dataset: 10.17632/zy2gmmcxp8.1), suggesting that the wounding-induced H₂O₂ transient burst is dependent on dual oxidase.

The level of epidermal H₂O₂ regulates CDC-42 clustering after wounding

As the H₂O₂ signal was reduced below the baseline after the initial burst, while the CDC-42 clusters continued to grow after wounding (Figure S4A), we then examined whether the H₂O₂ signal affects CDC-42 clustering. Interestingly, loss of function of *duox-2* significantly increased the number and size of the GFP::CDC-42 clusters (Figures 4A–4C; Figures S4D and S4E; Video S23 with the Mendeley dataset: 10.17632/zy2gmmcxp8.1). CDC-42 cluster number in the *duox-2* mutants was ~2-fold higher than that in the wild-type (WT) at 5 min after wounding (Figure 4B). In addition, the CDC-42 cluster size in the *duox-2* mutant was also ~3.4 times larger than in the WT (Figure 4C). Thus, the loss of function of *duox-2* reduces H₂O₂ levels and increases CDC-42 cluster formation upon wounding.

We further examined CDC-42 clustering in the H₂O₂ detoxifying mutants. Peroxidase and catalase are the primary metabolic enzymes for converting H₂O₂ to H₂O (Shadel and Horvath, 2015) (Figure S2B). *C. elegans* encodes three catalases and three peroxiredoxin-type peroxidases (Johnston and Ebert, 2012). We found that the number, size, and fluorescence intensity of CDC-42 clusters after wounding was significantly reduced in *prdx-2* or *ctl-1,2,3* (triple catalase gene knockout) deletion mutants compared with WT (Figures 4A–4C; Figures S4C, S4D, and S4F–S4H; Video S24 with the Mendeley dataset: 10.17632/zy2gmmcxp8.1). Consistent with these findings, GFP::WSP-1 recruitment was also significantly increased in the *duox-2* mutant but reduced in the *ctl-1,2,3* mutant (Figures S4I and S4J). Moreover, treatment with *tert*-Butyl hydroperoxide (tBOOH), a stable analog of H₂O₂ (Bartosz et al., 1997) (Figure S4B), significantly inhibited GFP::CDC-42 clustering after wounding (Figures S4K and S4L). In FRAP experiments, GFP::CDC-42 clusters displayed normal recovery in the *duox-2* mutants but not in either *prdx-2* or *ctl-1,2,3* mutants (Figures 4E and 4F; Video S25 with the Mendeley dataset: 10.17632/zy2gmmcxp8.1). Together, these results suggest that high H₂O₂ level inhibits the clustering of CDC-42 and subsequent recruitment of WSP-1.

The reduction of H₂O₂ enhances actin polymerization-based wound closure

Next, we investigated whether H₂O₂ signaling affects actin polymerization-based wound closure. Loss of function of *duox-2*, as well as of *bli-3*, led to enhanced wound closure with a smaller actin ring at 1 h.p.w. (Figures 5A and 5B; Figures S5A and S5B; Video S26 with the Mendeley dataset: 10.17632/zy2gmmcxp8.1), a finding consistent with the enhancement of CDC-42 clustering in these mutants (Figures 4A–4C). Conversely, overexpression of *duox-2(+)* led to delayed wound closure in the WT and rescued the rapid wound closure in the *duox-2* mutant (Figures 5A and 5B). Moreover, tBOOH treatment delayed actin polymerization in WT, as previously reported (Xu and Chisholm, 2014a), and suppressed the faster wound closure in *duox-2* and *bli-3* mutant animals (Figure 5B; Figure S5C). Conversely, *ctl-1,2,3* mutant displayed significant inhibition of actin polymerization (Figures 5C and 5D), while *ctl-1,2,3(+)* overexpression (Doonan et al., 2008) enhanced actin polymerization at the wound site (Figures 5C and 5D). Collectively, these results indicate that reduced cytosolic H₂O₂ levels enhance actin-based wound closure, consistent with our finding that reduced cytosolic H₂O₂ levels increase CDC-42 cluster formation.

Membrane attachment of CDC-42 is required for its rapid clustering upon wounding

To determine how wounding induces CDC-42 clustering, we examined whether this requires membrane attachment as the clusters colocalize with the membrane (Figures S1F and S1G). The CAAX motif mediates CDC-42 association to the plasma membrane via prenylation of Cys residue at the 188 position (Roberts et al., 2008) (Figure 6A). We thus generated a CDC-42 variant with C188A (Cys→Ala) mutation (Figure 6B; Figure S6A). The fluorescence signal for the GFP::CDC-42^{C188A} mutant variant was distinct from that of GFP::CDC-42^{WT} in two ways: it was diffused throughout the cytosol before wounding and did not form clusters after wounding (Figure 6B; Figure S6A; Video S27 with the Mendeley dataset: 10.17632/zy2gmmcxp8.1), suggesting that CAAX motif-mediated membrane attachment is essential for CDC-42 clustering. To confirm this, we performed epidermal-specific RNAi to knock down orthologs of enzymes implicated in prenylation,

such as *fnta-1*, *fntb-1*, *ggtb-1*, *fdps-1*, and *Y48E1B3* (Rauthan and Pilon, 2011). We observed that only knockdown of *fdps-1*, which encodes *C. elegans* farnesyl diphosphate synthetase, significantly reduced the CDC-42 membrane localization and clustering before and after wounding (Figure 6B; Figures S6B and S6C; Video S28 with the Mendeley dataset: 10.17632/zy2gmmcxp8.1). Conversely, knockdown of *rhi-1*, the *C. elegans* ortholog of rhoGDI required for the prenylated CDC-42 anchoring in the cytosol (Lin et al., 2003), resulted in a significant increase of the CDC-42 clustering after wounding (Figure 6C; Video S29 with the Mendeley dataset: 10.17632/zy2gmmcxp8.1). Collectively, these observations established that the prenylation-mediated membrane attachment of CDC-42 is necessary for cluster formation.

The C terminus CDC-42 contains multiple positively charged lysines (KKKK) (Figure 6A), which resemble polybasic regions (PBRs) that can mediate cation-phospholipid interactions that enhance CDC-42 family protein localization at the membrane (Yeung et al., 2008). To determine whether the *C. elegans* CDC-42 C-terminal PBR domain is required for clustering *in vivo*, we generated two CDC-42 PBR variants, mutating KKKK to less positively charged histidines (HHHH) or to hydrophobic alanines (AAAA) (Figure 6D; Figure S6D). Compared with CDC-42^{WT}, both variants displayed significant decreases in the number, size, and intensity of the CDC-42 cluster after wounding (Figures 6D and 6E). Moreover, expression of GFP fused with CAAX motif alone showed few puncta formation after wounding, while expression of an additional PBR further increased cluster formation (Figures S6D and S6E; Video S30 with the Mendeley dataset: 10.17632/zy2gmmcxp8.1). Collectively, these observations suggest that the CDC-42 C-terminal PBR facilitates CAAX motif-mediated membrane attachment and clustering in an additive manner (Figure 6F).

Cys18 and Cys105 within CDC-42 are required for sensing H₂O₂ and clustering

We then sought to determine how H₂O₂ negatively regulates CDC-42 clustering in response to wounding. Cys residues function as detectors of redox status in cells; this amino acid reacts with ROS to form disulfide bonds (Barford, 2004; Mitchell et al., 2013) (Figure 7A). We thus mutated all other five Cys residues in the CDC-42 and then examined the post-wounding clustering (Figures S7A and S7B). Two Cys mutants, C18A and C105A, showed dramatic increases in the number and size of CDC-42 clusters, while other Cys variants, including C6A, C81A, and C157A, did not significantly affect the formation of the cluster of GFP::CDC-42 (Figures S7C and S7D), suggesting that Cys18 and Cys105 are the key residues for CDC-42 inhibition by H₂O₂. To confirm this, we generated epidermal-specific single-copy insertion of GFP::CDC-42^{C18A} and GFP::CDC-42^{C105A} and compared their clustering with the GFP::CDC-42^{WT}. We found that the number and intensity of clusters were significantly increased in C18A and C105A mutants (Figures S7E and S7F; Video S31 with the Mendeley dataset: 10.17632/zy2gmmcxp8.1), confirming that these two Cys are required for the inhibition of CDC-42 clustering.

Cys oxidation and reversible disulfide bond formation are common post-translational modifications of a protein that responds to endogenous redox signals (Mitchell et al., 2013) (Figure 7A). We thus analyzed the recombinant expression of worm CDC-42 proteins using mass spectrometry and detected disulfide bonds between Cys18-Cys105 and Cys105-

Cys105 (Figure 7B; Figures S7G and S7H), suggesting that CDC-42 potentially forms intermolecular disulfide bonds via both these residues. Intermolecular disulfide bonds can increase the size of a protein; we thus performed SDS-PAGE gel analysis of GFP::CDC-42 recombinant protein and observed GFP::CDC-42 to migrate at a significantly larger size than predicted (Figure 7C), which was sensitive to reduction by dithiothreitol (DTT), consistent with oligomerization due to intermolecular disulfide bond formation (Figure 7B).

To determine whether Cys18 and Cys105 for CDC-42 are involved in response to the H₂O₂ signal, we generated knockin *GFP::CDC-42^{C18A}* and *GFP::CDC-42^{C105A}* mutant alleles at the endogenous *cdc-42* locus (Figure 7D). GFP::CDC-42^{C18A} and GFP::CDC-42^{C105A} formed more clusters compared with CDC-42^{WT} after wounding (Figures 7D–7F; Video S32 with the Mendeley dataset: 10.17632/zy2gmmcxp8.1). Importantly, H₂O₂ analog tBOOH treatment inhibited the formation of the clusters in GFP::CDC-42^{WT} but not in GFP::CDC-42^{C18A} and GFP::CDC-42^{C105A} mutant animals (Figures 7D–7F). Consistent with this, loss of function of catalase reduced GFP::CDC-42 clustering in WT, but not in either C18A or C105A mutants (Figures S7I and S7J), while GFP::CDC-42 clustering was not further enhanced in the *duox-2* mutant (Figures S7K and S7L). Together, these results indicate that Cys18 and Cys105 are required for the inhibition of CDC-42 clustering by H₂O₂.

We then determined how CDC-42^{C18A} and CDC-42^{C105A} variants affect cluster formation. As membrane attachment of CDC-42 is required for its clustering after wounding (Figure 6F), we examined the membrane association of CDC-42^{C18A} and CDC-42^{C105A} variants. We performed subcellular fractionation analysis of membrane and cytosol from whole animals and detected CDC-42 using western blot (Figure 7G). We observed that CDC-42 was associated with both membrane and cytosol in unwounded WT (membrane-to-cytosolic [M/C] ratio = ~ 0.31); importantly, the M/C ratios of CDC-42^{C18A} and CDC-42^{C105A} were significantly increased to 1.47 and 2.15, respectively (Figure 7G), while that of CDC-42^{C188A} variant was decreased to 0 (Figure 7G). Moreover, the colocalization of GFP fused with CDC-42^{C18A} and CDC-42^{C105A} with myr::mKate2 also significantly increased compared with GFP::CDC-42^{WT} (Figures S7M and S7N). Together, these results suggest that the C18A and C105A mutations cause increased membrane association in the unwounded state, resulting in enhanced CDC-42 clustering after wounding.

Finally, in light of our findings that CDC-42 clustering promotes wound closure, we examined the effects of CDC-42^{C18A} and CDC-42^{C105A} mutation in actin polymerization during wound closure *in vivo*. Consistent with enhanced CDC-42 clustering in these variants (Figures 7D–7F), we observed that the GFP::CDC-42^{C18A} and GFP::CDC-42^{C105A} mutants exhibited faster wound closure resulting in smaller actin rings at 1 h.p.w. than the GFP::CDC-42^{WT} animals (Figure 7H). Together, these results suggest that the enhanced clustering ability of CDC-42 C18A and C105A mutants promotes actin polymerization-based wound closure.

DISCUSSION

Collectively, our findings suggest a model in which wounding induces a rapid local burst of H₂O₂ to regulate CDC-42 clustering, which promotes wound repair in the *C. elegans* epidermis (Figure 7I). We show that CDC-42 clustering is dependent on membrane attachment via the C-terminal PBR and CAAX motif, allowing coordinated interactions of CDC-42 with lipid structure in the membrane. H₂O₂ signal inhibits CDC-42 clustering via disulfide bond formation between Cys18 and Cys105, possibly providing a fine-tuning mechanism for CDC-42 over-activation during the early stages of wound closure. Our findings collectively support a model wherein the association of CDC-42 and membrane drives damage-coupled macroscopic biomolecular clustering to promote actin polymerization-based wound closure.

Our findings also explain the mechanism through which an immediate wound response to H₂O₂ yields transitions in physically and functionally distinct states of the CDC-42 protein, thus connecting responses at disparate scales in the epidermis. Further exploration of CDC-42 clustering should yield additional insights into the reorganization of the plasma membrane after wounding. Wounding is known to trigger an immediate increase in cellular Ca²⁺ and ATP levels and to boost electrical signals (Cordeiro and Jacinto, 2013; Enyedi and Niethammer, 2015; Niethammer, 2016), which could also contribute to the rapid membrane-mediated clustering that we discovered for CDC-42. Wounding is also known to induce an immediate reduction of mechanical tension in the plasma membrane (Harn et al., 2019; Zulueta-Coarasa and Fernandez-Gonzalez, 2017). Whether and how CDC-42 senses membrane tension change upon wounding remains to be investigated.

Previous studies have shown that CDC-42 is necessary for cell polarity, chemotaxis, and cell migration, and CDC-42 induces most of the WSP-1-mediated actin polymerization required for cell motility (Burkel et al., 2012; Osmani et al., 2010; Yang et al., 2016). Our finding that CDC-42 clustering is induced over the zone surrounding the wound region is consistent with the previous observation that CDC-42 signal exhibits a local excitable characteristic of the activity required for chemotaxis (Yang et al., 2016). Interestingly, wounding-induced CDC-42 clusters recruit WSP-1 into propagating waves at the wound site (Video S6 with the Mendeley dataset: 10.17632/zy2gmmcxp8.1), similar to the notion that the WAVE complex regulates propagating actin waves to “organize the leading edge of motile immune cells” (Weiner et al., 2007). It will be interesting to determine if the local clustering of CDC-42 triggers wave-like actin polymerization around a specific wound site.

The CDC-42 C terminus attaches to the lipid membrane on the basis of post-translational modification (prenylation) and cation-phospholipid interactions (Yeung et al., 2008). Recent findings have suggested that wound-induced influx of Ca²⁺ can change the dynamics and organization of negatively charged lipids, promoting a membrane phase transition (Lin et al., 2020). We speculate that wounding induces conformational changes in the lipid bilayer, for example, the formation of PIP₂ or PIP₃ clusters (Pickering et al., 2013), which may immediately recruit prenylated CDC-42 to the membrane and is enhanced by the cation-phospholipid interaction. It will be interesting to investigate whether clustering of

CDC-42 at the membrane involves wound-triggered changes in membrane lipid composition or dynamics.

H₂O₂ has long been considered a damage signal by protein oxidation (Hernández-Oñate and Herrera-Estrella, 2015). In the present study, we found that H₂O₂ regulates the clustering of CDC-42 *in vivo*. Recent findings have shown that oxidation of methionine in Ataxin-2/Pbp1 in yeast and Cys in transcription factor TMF in tomato function as H₂O₂ sensors to function via phase separation (Huang et al., 2021; Kato et al., 2019). This, viewed alongside our results, suggests that protein oxidation by endogenous ROS signals may function widely to regulate protein localization and activity response to various stimuli.

H₂O₂ bursts occur after wounding in diverse organisms, including plants (Hernández-Oñate and Herrera-Estrella, 2015; Niethammer, 2016; Suzuki and Mittler, 2012), and these bursts are required for damage detection and immune cell recruitment to wound sites, as well as wound healing in *Drosophila* (Hunter et al., 2018; Ponte et al., 2020) and regeneration in *Xenopus* (Love et al., 2013) and zebrafish (Yoo et al., 2011). We have found a local burst of H₂O₂ immediately after laser wounding of the *C. elegans* syncytial epidermis. For the transient burst detected using simultaneous imaging and laser wounding, it is possible that H₂O₂ may be induced and released to the extracellular matrix immediately after wounding. This signal is likely different in nature from the previously reported wounding-induced H₂O₂ signals in studies of multicellular epithelial injury (Niethammer et al., 2009; Pase et al., 2012). We speculate that H₂O₂ may function to locally and temporally modulate CDC-42 activity to ensure controlled actin polymerization during the early stage of wound repair. Thus, our study suggests how wounding-induced H₂O₂ production links to Rho GTPases sensation and cytoskeleton reorganization in regulating wound repair and regeneration.

Limitations of study

We revealed that epidermal wounding triggers immediate clustering of CDC-42, which recruits the downstream target WSP-1 to promote wound closure in *C. elegans*. We further showed that the two Cys in CDC-42 (Cys18 and Cys105) might sense the wounding-induced H₂O₂ signal via intermolecular disulfide bond formation and negatively regulates CDC-42 clustering. However, the underlying mechanism by which the CDC-42 Cys are sensing H₂O₂ to regulate the clustering of CDC-42 remains elusive. The issue could be addressed in the future by using single-molecule biochemical approaches, including CDC-42, CDC-42 mutants, and WSP-1, with treatment with H₂O₂ or its antagonists.

STAR*METHODS

RESOURCE AVAILABILITY

Lead contact—Further information and requests for resources and reagents should be directed to and will be fulfilled by the Lead Contact, Suhong Xu (shxu@zju.edu.cn).

Materials availability—All requests for resources and reagents should be directed to and will be fulfilled by the Lead Contact.

Data and code availability

- The Mass Spectrometric data during this study are publicly available at ProteomeXchange (PASS01707) as of the date of publication. The supplementary videos have been deposited at Mendeley Data (<https://doi.org/10.17632/zy2gmmcxp8.1>) and are publicly available. All other reagents generated in this study are available from the Lead Contact upon request.
- This paper does not report original code.
- Any additional information required to reanalyze the data reported in this work paper is available from the Lead Contact upon request.

EXPERIMENTAL MODEL AND SUBJECT DETAILS

C. elegans strains were cultured on the nematode growth medium (NGM) plates seeded with *E. coli* OP50 following standard protocols at 20–22.5°C, unless otherwise indicated. The N2 Bristol strain was used as the WT strain. Standard procedures were used to construct new strains, including CRISPR-Cas9 genome editing method, and these strains were genotyped by PCR and sequencing. Previously described transgenes or mutations include *duox-2* (*ok1775*), *bli-3* (*e767*), *prdx-2* (*gk169*) are from CGC, and *GFP::wsp-1a* (*cas723*) (Wu et al., 2017) is kindly provided by Dr. Guangshuo Ou. Standard microinjection methods were used to generate transgenic animals carrying extrachromosomal arrays (*zjuEx*). Single-copy insertion of arrays (*zjuSi*) and GFP fusion knock-in strains were generated using CRISPR-Cas9 genome editing methods, as described previously (Xu et al., 2016). *ctl-1,2,3(zju181)*, *GFP::cdc-42^{wt} (zju208)*, *GFP::cdc-42^{C18A} (zju210)*, *GFP::cdc-42^{C105A} (zju223)* were generated in this project. All strains that were used in this work are summarized in the Key Resources Table and Table S1.

METHOD DETAILS

Constructs and transgenic worms—For extrachromosomal array transgenic worms, 10 ng/μl plasmids and 50 ng/μl co-injection marker (*Pttx-3-RFP* or *Pttx-3-GFP*) were injected into N2 animals. CRISPR-Cas9 based single-copy insertion was performed as described previously (Fu et al., 2020). Briefly, Cas9, insertion plasmids, and sgRNA targeted on a specific chromosome were co-injected into N2 animals and screened for the insertion via PCR followed by sequencing. The insertion site of SCI is the site of ttTi4348 on Chr I and ttTi5605 on Chr II. New single-copy insertion strains are: *Pcol-19-LifeAct::TagBFP(zjuSi83)II*, *Pcol-19-roGFP2::Orp1(zjuSi16) I*, *Pcol-19-GFP::CDC-42(zjuSi2) I*, *Pcol-19-mKate2::CDC-42(zjuSi108) I*, *Pcol-19-GFP::CDC-42^{C18A} (zjuSi138) I*, *Pcol-19-GFP::CDC-42^{C105A} (zjuSi190) I*, *Pcol-19-GFP::CDC-42^{C18A;C105A} (zjuSi285) I*, *Pcol-19-GFP::wsp-1 (zjuSi173) II*. New strains, constructs, and primers used in this study are listed in the Key Resource Table and Tables S1–S3.

CRISPR-Cas9 mediated gene knock-in—*GFP::cdc-42^{wt} (zju208)*, *GFP::cdc-42^{C18A} (zju210)*, and *GFP::cdc-42^{C105A} (zju223)* knock-in animals were generated by using the CRISPR-Cas9 system as described previously (Meng et al., 2020). Briefly, two repair templates (each with 1500 bp) were cloned by Gibson assembly within pDD282

plasmid and site mutagenesis modification for point mutation. The templates include the *cdc-42* 5' UTR (~1500 bp), GFP codon sequence (with ATG), and around 1500 bp from the beginning of *cdc-42* sequence (without ATG). Mixed plasmids of pSX1480 (GFP::CDC-42 repair template), pSX1761 (*GFP::CDC-42^{C18A}* KI repair template), or pSX1909 (*GFP::CDC-42^{C105A}* KI repair template) 50 ng/μl, pSX1484 and pSX1485 as pU6-sgRNAs 30 ng/μl respectively, pSX524 (*Peft-3-cas9-NLS-pU6-dpy-10* sgRNA) 50 ng/μl as well as pSX424 (*Pmyo-3-cherry*) 5 ng/μl, pSX375 (*Pmyo-2-cherry*) 2.5 ng/μl and pSX379 10 ng/μl (*Prab-3-cherry*) as co-injection red marker were injected into N2 worms. Worms were cultured at 25°C for 2~3 days, and 3~5 dumpy/roller/red L4 or older worms were picked into a new fresh plate. F₂ animals carrying GFP signals with no red markers were picked and were let to lay eggs. Picked animals were then confirmed by PCR genotyping and sequencing. *dpy-10* mutations on the genome were removed by outcrossing with N2. All these knock-in animals are superficially normal morphology as WT.

Catalases knock out—*ctl-1,2,3(zju181)* knockout strain was generated by the CRISPR-Cas9 system as described previously (Xu et al., 2016). Mixed plasmids of pSX799 (*pU6-BseRI-BseRI-sgRNA-ctl-1,2,3* up) 50 ng/μl, pSX801 (*pU6-BseRI-BseRI-sgRNA-ctl-1,2,3* down) and pSX524 (*Peft-3-cas9-NLS-pU6-dpy-10* sgRNA) 50 ng/μl were injected into N2. Worms were cultured at 25°C for 2~3 days, and every 3~5 dumpy/roller/L4 or elder worms were picked into a new fresh plate. F₂ animals were checked by genotyping and outcrossed to N2 before experiments.

Drug treatment—All drugs were dropped onto the OP50 bacterial lawn from a high concentration stock and allowed to dry for 1~2 hours at room temperature before transferring the young adult animals. For prolong drug treatments, young adults were transferred to freshly made NGM drug plates and incubated overnight at 20°C before needle wounding. *tert*-butyl hydroperoxide (tBOOH, B2633 Sigma) was dissolved in M9; the working concentration of tBOOH is 1 mM.

Wounding, repair, and survival assay—We wounded the epidermis of young adult stage animals using a Micropoint UV laser or needle. All images before and after wounding were taken using a spinning disk confocal microscope (Andor 100x, NA 1.46 objective). Actin ring quantitation and survival rate were performed as previously described (Xu and Chisholm, 2014b).

RNAi inactivation experiments in *C. elegans*—Animals were fed with double-stranded RNAs that correspond to the sequence of *cdc-42*, *wsp-1* as an experimental group, and L4440 empty vector as a control group. L4 stage animals were placed on RNAi plates overnight before doing the experiment as described previously (Xu and Chisholm, 2011). RNAi bacteria were obtained from the Ahringer feeding library.

roGFP2::Orp1 imaging and analysis—The cytosolic H₂O₂ was quantified through image analysis of specific H₂O₂ probe roGFP2::Orp1 as described previously (Morgan et al., 2011). Briefly, the single-copy insertion of *Pcol-19-roGFP2::Orp1(zjuSi16)* transgenic animals were used for wounding and imaging. Laser wounding images of roGFP2::Orp1 were taken using a spinning disk confocal microscope (Nikon) (100x, NA 1.46) with excitation

on 405 and 488 nm and emission on 525 nm filter. Images were imported into software *ImageJ* and converted to 32-bit. The range of threshold was set in both channels; the ratio of 405/488 indicates the local level of H₂O₂. To quantify the production of H₂O₂ upon wounding, region of interest (ROI) around wounds was selected, and the intensity ratio of 405/488 was measured in a stack.

Cluster size, number, and intensity quantification—All cluster analyses were performed in ImageJ. Background intensity was used as a threshold. The size, intensity, and the number of clusters were analyzed using Analyze Particles (a function in ImageJ software) automatically with minimum size at 0.2 square micrometers. The value of cluster size, number, and intensity was automatically calculated and analyzed using GraphPad. At least 20 wounded young adult animals were examined. For cluster number, 800 × 400-pixel around the wounded area was chosen for analysis. The size, number, and intensity change were quantified by mean with Standard Error of the Mean (SEM) included.

Fluorescence recovery after photobleaching (FRAP)—Fluorescence recovery after photobleaching (FRAP) experiment was performed on a spinning disk system as described previously (Meng et al., 2020). Briefly, the puncta were randomly selected and photobleached with 100% 405 nm laser transmission (405 nm 15 mW, argon laser power is 40 mW). Images were taken for 20 minutes with 10 s intervals and were analyzed by normalizing to the initial intensity before photobleaching. Number (n) refers to the number of photobleached puncta.

Immunostaining—Worms were fixed and stained by indirect immunofluorescence as previously described (Bosher et al., 2003). Animals were resuspended in PBST and incubated with primary antibody (CDC-42 Recombinant Rabbit Monoclonal Antibody, HUABIO, ET1701–7) overnight at 4°C. The samples were washed 3 times with PBST and incubated with a secondary antibody (anti-rabbit IgG, Multi Sciences; GAR007) for 1 hour at room temperature. The samples were then washed 3 times with PBST and observed with a spinning disk confocal microscope. The immunofluorescence images were representatives of three independent experiments.

Subcellular fractionation—Subcellular fractionation of *C. elegans* was performed as previously described (Norris et al., 2017) with few modifications. Briefly, animals with different genetic backgrounds were synchronized and cultured at 20°C until young adult stage, and then washed off from the plates with M9 buffer and resuspended in 200 µL lysis buffer [20 mM HEPES, PH 8.0, 20% (wt/vol) sucrose, 10% (vol/vol) glycerol, 1 mM EDTA, and 2% protease inhibitors]. Approximate 1,000 worms were then homogenized by tissue blender on ice. The debris of cuticles, tissue fragments, and nuclei were removed by centrifugation at 4°C and 1,000 g for 5 min. A total of 100 µL of the postnuclear lysate was centrifuged at 4°C and 16,000 g for 20 min until separated into pellets and soluble fractions. Pellets were reconstituted in 20 µL of lysis buffer as the plasma membrane fraction of worms, while the soluble fractions were described as cytosol parts. The relative ratio of target protein between in membrane fraction and in cytosol fraction was calculated by gray

value analysis after western blot. The same volume of the samples was loaded in the western blot. Rabbit polyclonal anti-GFP antibodies (MBL, #598) were used for blot.

Cell culture—HEK293 cells were maintained in a DMEM culture medium. Both media were supplemented with 10% fetal calf serum (FCS), 100 µg/ml of streptomycin, 100 IU/mL of penicillin, and 2 mM l-glutamine. Cells were cultivated at 37°C with 5% CO₂.

Protein expression and purification—CDC-42 cDNAs were PCR-amplified and cloned into pCMV vector to produce GFP-tag fused recombinant proteins. For eukaryotic expression, cells were then transiently transfected using PEI 40K (Mkbio, MX2205) with DNA:PEI ratio of 1:4 and cultured for 48 hours. The cells were harvested and resuspended in the lysis buffer (50 mM Na₂HPO₄, 400 mM NaCl, 0.3% Triton100) with protease inhibitors (0.3 mM PMSF, InStab™ protease Inhibitor Cocktail, 20124ES03, Teasen). Proteins with GFP-tagged CDC-42 were incubated with Anti-GFP agarose nanobeads (AlpaLife, KTSM1301), and the supernatant was eluted in 0.2 mM sodium citrate (pH 2.0), and then Tris-HCl (pH 9.5) was used to neutralize sodium citrate. Proteins were concentrated with PBS using 10 kDa concentration column, and the concentration was determined with Nanodrop (ThermoFisher).

Mass spectrometric analysis of protein disulfide bonds—Protein disulfide bond identification was performed as described before (Huang et al., 2021). Briefly, the purified recombinant CDC-42 proteins were evenly divided into two parts and digested with Trypsin and Trypsin+GluC, respectively. After digestion overnight, the samples were mixed and loaded after desalting with ZipTip. The digested samples were loaded into Orbitrap Fusion Lumos equipped with EASY-nLC 1200 (ThermoFisher) for liquid chromatography-tandem mass spectrometry (LC-MS/MS) analysis. The resolution of MS1 and MS2 scans were set to 120,000 and 15,000, respectively. The search engine pLink v.2.3.9 (<http://pfind.ict.ac.cn/software/pLink/index.html>) was used for disulfide linkage analysis (Chen et al., 2019). Both precursor mass and fragment tolerance were set at 20 ppm.

Imaging analysis—All the images were analyzed by using ImageJ software and its plugins (<https://imagej.nih.gov/ij/>).

QUANTIFICATION AND STATISTICAL ANALYSIS

All statistical analyses used GraphPad Prism 7 (La Jolla, CA). The Standard Error of the Mean (SEM) or Standard Deviation (SD) was used for bar charts plotted from the mean value of the data. Two-way comparisons used unpaired t test, one-way ANOVA for multiple comparisons, non-parametric Mann-Whitney test for two comparisons. Data were considered statistically different at $p < 0.05$. $p < 0.05$ is indicated with single asterisks, $p < 0.01$ with double asterisks, and $p < 0.001$ with triple asterisks. All experiments were repeated on separate days with separate, independent populations to confirm that results were reproducible. Additional statistical details of experiments, including sample size and replication, can be found in the figure legends.

Supplementary Material

Refer to Web version on PubMed Central for supplementary material.

ACKNOWLEDGMENTS

We thank Drs. Guangshuo Ou and Tobias P. Dick for reagents; Drs. Hong Zhang, Guangshuo Ou, Wei Liu, Bing Yang, and Yiting Zhou for comments on the manuscript; and Xu lab members for support and discussion. We thank the Plant Science Facility of the Institute of Botany, Chinese Academy of Sciences, for help with mass spectrometry. This work was supported by the National Natural Science Foundation of China (NSFC; grants 31671522, 31972891, and 91754111) to S.X. A.D.C. is supported by NIH grant R35 GM134970. Q.S. is supported by NSFC grant 91754113, and J.W.C. is supported by NSFC grant 31971237. Several *C. elegans* strains were provided by the Caenorhabditis Genetics Center (CGC), which is supported by the NIH Office of Research Infrastructure Programs (P40OD010440).

REFERENCES

- Banjade S, and Rosen MK (2014). Phase transitions of multivalent proteins can promote clustering of membrane receptors. *eLife* 3, e04123.
- Barford D (2004). The role of cysteine residues as redox-sensitive regulatory switches. *Curr. Opin. Struct. Biol* 14, 679–686. [PubMed: 15582391]
- Bartosz M, Kedziora J, and Bartosz G (1997). Antioxidant and prooxidant properties of captopril and enalapril. *Free Radic. Biol. Med* 23, 729–735. [PubMed: 9296449]
- Benink HA, and Bement WM (2005). Concentric zones of active RhoA and Cdc42 around single cell wounds. *J. Cell Biol* 168, 429–439. [PubMed: 15684032]
- Bosher JM, Hahn BS, Legouis R, Sookhareea S, Weimer RM, Gansmuller A, Chisholm AD, Rose AM, Bessereau JL, and Labouesse M (2003). The Caenorhabditis elegans vab-10 spectraplaklin isoforms protect the epidermis against internal and external forces. *J. Cell Biol* 161, 757–768. [PubMed: 12756232]
- Braeckman BP, Smolders A, Back P, and De Henau S (2016). In vivo detection of reactive oxygen species and redox status in Caenorhabditis elegans. *Antioxid. Redox Signal* 25, 577–592. [PubMed: 27306519]
- Burkel BM, Benink HA, Vaughan EM, von Dassow G, and Bement WM (2012). A Rho GTPase signal treadmill backs a contractile array. *Dev. Cell* 23, 384–396. [PubMed: 22819338]
- Chen ZL, Meng JM, Cao Y, Yin JL, Fang RQ, Fan SB, Liu C, Zeng WF, Ding YH, Tan D, et al. (2019). A high-speed search engine pLink 2 with systematic evaluation for proteome-scale identification of cross-linked peptides. *Nat. Commun* 10, 3404. [PubMed: 31363125]
- Clark AG, Miller AL, Vaughan E, Yu HY, Penkert R, and Bement WM (2009). Integration of single and multicellular wound responses. *Curr. Biol* 19, 1389–1395. [PubMed: 19631537]
- Cordeiro JV, and Jacinto A (2013). The role of transcription-independent damage signals in the initiation of epithelial wound healing. *Nat. Rev. Mol. Cell Biol* 14, 249–262.
- de Oliveira S, López-Muñoz A, Candel S, Pelegrín P, Calado Â, and Mulero V (2014). ATP modulates acute inflammation in vivo through dual oxidase 1-derived H₂O₂ production and NF- κ B activation. *J. Immunol* 192, 5710–5719. [PubMed: 24842759]
- de Oliveira S, Boudinot P, Calado Â, and Mulero V (2015). Duox1-derived H₂O₂ modulates Cxcl8 expression and neutrophil recruitment via JNK/c-JUN/AP-1 signaling and chromatin modifications. *J. Immunol* 194, 1523–1533. [PubMed: 25582859]
- Doonan R, McElwee JJ, Matthijssens F, Walker GA, Houthoofd K, Back P, Matscheski A, Vanfleteren JR, and Gems D (2008). Against the oxidative damage theory of aging: superoxide dismutases protect against oxidative stress but have little or no effect on life span in Caenorhabditis elegans. *Genes Dev* 22, 3236–3241. [PubMed: 19056880]
- Edens WA, Sharling L, Cheng G, Shapira R, Kinkade JM, Lee T, Edens HA, Tang X, Sullards C, Flaherty DB, et al. (2001). Tyrosine cross-linking of extracellular matrix is catalyzed by Duox, a multidomain oxidase/oxidoreductase with homology to the phagocyte oxidase subunit gp91phox. *J. Cell Biol* 154, 879–891. [PubMed: 11514595]

- Eming SA, Wynn TA, and Martin P (2017). Inflammation and metabolism in tissue repair and regeneration. *Science* 356, 1026–1030. [PubMed: 28596335]
- Enyedi B, and Niethammer P (2015). Mechanisms of epithelial wound detection. *Trends Cell Biol* 25, 398–407. [PubMed: 25813429]
- Fu H, Zhou H, Yu X, Xu J, Zhou J, Meng X, Zhao J, Zhou Y, Chisholm AD, and Xu S (2020). Wounding triggers MIRO-1 dependent mitochondrial fragmentation that accelerates epidermal wound closure through oxidative signaling. *Nat. Commun* 11, 1050. [PubMed: 32103012]
- Gurtner GC, Werner S, Barrandon Y, and Longaker MT (2008). Wound repair and regeneration. *Nature* 453, 314–321. [PubMed: 18480812]
- Harn HI, Ogawa R, Hsu CK, Hughes MW, Tang MJ, and Chuong CM (2019). The tension biology of wound healing. *Exp. Dermatol* 28, 464–471. [PubMed: 29105155]
- Hernández-Oñate MA, and Herrera-Estrella A (2015). Damage response involves mechanisms conserved across plants, animals and fungi. *Curr. Genet* 61, 359–372. [PubMed: 25572693]
- Higgs HN, and Pollard TD (2000). Activation by Cdc42 and PIP(2) of Wiskott-Aldrich syndrome protein (WASp) stimulates actin nucleation by Arp2/3 complex. *J. Cell Biol* 150, 1311–1320. [PubMed: 10995437]
- Huang X, Chen S, Li W, Tang L, Zhang Y, Yang N, Zou Y, Zhai X, Xiao N, Liu W, et al. (2021). ROS regulated reversible protein phase separation synchronizes plant flowering. *Nat. Chem. Biol* 17, 549–557. [PubMed: 33633378]
- Hunter MV, Willoughby PM, Bruce AEE, and Fernandez-Gonzalez R (2018). Oxidative stress orchestrates cell polarity to promote embryonic wound healing. *Dev. Cell* 47, 377–387.e4. [PubMed: 30399336]
- Johnston AD, and Ebert PR (2012). The redox system in *C. elegans*, a phylogenetic approach. *J. Toxicol* 2012, 546915. [PubMed: 22899914]
- Kato M, Yang YS, Sutter BM, Wang Y, McKnight SL, and Tu BP (2019). Redox state controls phase separation of the yeast Ataxin-2 protein via reversible oxidation of its methionine-rich low-complexity domain. *Cell* 177, 711–721.e8. [PubMed: 30982603]
- Li P, Banjade S, Cheng HC, Kim S, Chen B, Guo L, Llaguno M, Hollingsworth JV, King DS, Banani SF, et al. (2012). Phase transitions in the assembly of multivalent signalling proteins. *Nature* 483, 336–340. [PubMed: 22398450]
- Lin Q, Fuji RN, Yang W, and Cerione RA (2003). RhoGDI is required for Cdc42-mediated cellular transformation. *Curr. Biol* 13, 1469–1479. [PubMed: 12956948]
- Lin YC, Chipot C, and Scheuring S (2020). Annexin-V stabilizes membrane defects by inducing lipid phase transition. *Nat. Commun* 11, 230. [PubMed: 31932647]
- Love NR, Chen Y, Ishibashi S, Kritsiligkou P, Lea R, Koh Y, Gallop JL, Dorey K, and Amaya E (2013). Amputation-induced reactive oxygen species are required for successful *Xenopus* tadpole tail regeneration. *Nat. Cell Biol* 15, 222–228. [PubMed: 23314862]
- Martin P, and Lewis J (1992). Actin cables and epidermal movement in embryonic wound healing. *Nature* 360, 179–183. [PubMed: 1436096]
- Martínez-Navarro FJ, Martínez-Morcillo FJ, de Oliveira S, Candel S, Cabas I, García-Ayala A, Martínez-Menchón T, Corbalán-Vélez R, Mesa-Del-Castillo P, Cayuela ML, et al. (2020). Hydrogen peroxide in neutrophil inflammation: lesson from the zebrafish. *Dev. Comp. Immunol* 105, 103583. [PubMed: 31862296]
- Meitzler JL, Brandman R, and Ortiz de Montellano PR (2010). Perturbed heme binding is responsible for the blistering phenotype associated with mutations in the *Caenorhabditis elegans* dual oxidase 1 (DUOX1) peroxidase domain. *J. Biol. Chem* 285, 40991–41000. [PubMed: 20947510]
- Meng X, Yang Q, Yu X, Zhou J, Ren X, Zhou Y, and Xu S (2020). Actin polymerization and ESCRT trigger recruitment of the fusogens syntaxin-2 and EFF-1 to promote membrane repair in *C. elegans*. *Dev. Cell* 54, 624–638.e5. [PubMed: 32668210]
- Mitchell L, Hobbs GA, Aghajanian A, and Campbell SL (2013). Redox regulation of Ras and Rho GTPases: mechanism and function. *Antioxid. Redox Signal* 18, 250–258. [PubMed: 22657737]
- Morgan B, Sobotta MC, and Dick TP (2011). Measuring E(GSH) and H₂O₂ with roGFP2-based redox probes. *Free Radic. Biol. Med* 51, 1943–1951. [PubMed: 21964034]

- Mosteiro L, Pantoja C, Alcazar N, Marión RM, Chondronasiou D, Rovira M, Fernandez-Marcos PJ, Muñoz-Martin M, Blanco-Aparicio C, Pastor J, et al. (2016). Tissue damage and senescence provide critical signals for cellular reprogramming in vivo. *Science* 354, aaf4445. [PubMed: 27884981]
- Niethammer P (2016). The early wound signals. *Curr. Opin. Genet. Dev* 40, 17–22. [PubMed: 27266971]
- Niethammer P, Grabher C, Look AT, and Mitchison TJ (2009). A tissue-scale gradient of hydrogen peroxide mediates rapid wound detection in zebrafish. *Nature* 459, 996–999. [PubMed: 19494811]
- Norris A, Tammineni P, Wang S, Gerdes J, Murr A, Kwan KY, Cai Q, and Grant BD (2017). SNX-1 and RME-8 oppose the assembly of HGRS-1/ESCRT-0 degradative microdomains on endosomes. *Proc. Natl. Acad. Sci. U S A* 114, E307–E316. [PubMed: 28053230]
- Osmani N, Peglion F, Chavrier P, and Etienne-Manneville S (2010). Cdc42 localization and cell polarity depend on membrane traffic. *J. Cell Biol* 191, 1261–1269. [PubMed: 21173111]
- Pase L, Layton JE, Wittmann C, Ellett F, Nowell CJ, Reyes-Aldasoro CC, Varma S, Rogers KL, Hall CJ, Keightley MC, et al. (2012). Neutrophil-delivered myeloperoxidase dampens the hydrogen peroxide burst after tissue wounding in zebrafish. *Curr. Biol* 22, 1818–1824. [PubMed: 22940471]
- Pickering K, Alves-Silva J, Goberdhan D, and Millard TH (2013). Par3/Bazooka and phosphoinositides regulate actin protrusion formation during *Drosophila* dorsal closure and wound healing. *Development* 140, 800–809. [PubMed: 23318638]
- Ponte S, Carvalho L, Gagliardi M, Campos I, Oliveira PJ, and Jacinto A (2020). Drp1-mediated mitochondrial fission regulates calcium and F-actin dynamics during wound healing. *Biol. Open* 9, bio048629. [PubMed: 32184231]
- Qiu X, Andresen K, Lamb JS, Kwok LW, and Pollack L (2008). Abrupt transition from a free, repulsive to a condensed, attractive DNA phase, induced by multivalent polyamine cations. *Phys. Rev. Lett* 101, 228101. [PubMed: 19113524]
- Ramachandran H, Banerjee B, Greenberger PA, Kelly KJ, Fink JN, and Kurup VP (2004). Role of C-terminal cysteine residues of *Aspergillus fumigatus* allergen Asp f 4 in immunoglobulin E binding. *Clin. Diagn. Lab. Immunol* 11, 261–265. [PubMed: 15013973]
- Rauthan M, and Pilon M (2011). The mevalonate pathway in *C. elegans*. *Lipids Health Dis* 10, 243. [PubMed: 22204706]
- Roberts PJ, Mitin N, Keller PJ, Chenette EJ, Madigan JP, Currin RO, Cox AD, Wilson O, Kirschmeier P, and Der CJ (2008). Rho family GTPase modification and dependence on CAAX motif-signaled posttranslational modification. *J. Biol. Chem* 283, 25150–25163. [PubMed: 18614539]
- Sawa M, Suetsugu S, Sugimoto A, Miki H, Yamamoto M, and Takenawa T (2003). Essential role of the *C. elegans* Arp2/3 complex in cell migration during ventral enclosure. *J. Cell Sci* 116, 1505–1518. [PubMed: 12640035]
- Shadel GS, and Horvath TL (2015). Mitochondrial ROS signaling in organismal homeostasis. *Cell* 163, 560–569. [PubMed: 26496603]
- Sonnemann KJ, and Bement WM (2011). Wound repair: toward understanding and integration of single-cell and multicellular wound responses. *Annu. Rev. Cell Dev. Biol* 27, 237–263. [PubMed: 21721944]
- Suzuki N, and Mittler R (2012). Reactive oxygen species-dependent wound responses in animals and plants. *Free Radic. Biol. Med* 53, 2269–2276. [PubMed: 23085520]
- Weiner OD, Marganski WA, Wu LF, Altschuler SJ, and Kirschner MW (2007). An actin-based wave generator organizes cell motility. *PLoS Biol* 5, e221. [PubMed: 17696648]
- Wong VW, Longaker MT, and Gurtner GC (2012). Soft tissue mechano-transduction in wound healing and fibrosis. *Semin. Cell Dev. Biol* 23, 981–986. [PubMed: 23036529]
- Wood W, Jacinto A, Grose R, Woolner S, Gale J, Wilson C, and Martin P (2002). Wound healing recapitulates morphogenesis in *Drosophila* embryos. *Nat. Cell Biol* 4, 907–912. [PubMed: 12402048]
- Wu D, Chai Y, Zhu Z, Li W, Ou G, and Li W (2017). CED-10-WASP-Arp2/3 signaling axis regulates apoptotic cell corpse engulfment in *C. elegans*. *Dev. Biol* 428, 215–223. [PubMed: 28602951]
- Xu S, and Chisholm AD (2011). A Gαq-Ca²⁺ signaling pathway promotes actin-mediated epidermal wound closure in *C. elegans*. *Curr. Biol* 21, 1960–1967. [PubMed: 22100061]

- Xu S, and Chisholm AD (2014a). *C. elegans* epidermal wounding induces a mitochondrial ROS burst that promotes wound repair. *Dev. Cell* 31, 48–60. [PubMed: 25313960]
- Xu S, and Chisholm AD (2014b). Methods for skin wounding and assays for wound responses in *C. elegans*. *J. Vis. Exp* (94), 51959.
- Xu S, Wang Z, Kim KW, Jin Y, and Chisholm AD (2016). Targeted mutagenesis of duplicated genes in *Caenorhabditis elegans* using CRISPR-Cas9. *J. Genet. Genomics* 43, 103–106. [PubMed: 26924693]
- Yang HW, Collins SR, and Meyer T (2016). Locally excitable Cdc42 signals steer cells during chemotaxis. *Nat. Cell Biol* 18, 191–201. [PubMed: 26689677]
- Yeung T, Gilbert GE, Shi J, Silvius J, Kapus A, and Grinstein S (2008). Membrane phosphatidylserine regulates surface charge and protein localization. *Science* 319, 210–213. [PubMed: 18187657]
- Yoo SK, Starnes TW, Deng Q, and Huttenlocher A (2011). Lyn is a redox sensor that mediates leukocyte wound attraction in vivo. *Nature* 480, 109–112. [PubMed: 22101434]
- Zulueta-Coarasa T, and Fernandez-Gonzalez R (2017). Tension (re)builds: biophysical mechanisms of embryonic wound repair. *Mech. Dev* 144 (Pt A), 43–52. [PubMed: 27989746]

Highlights

- Wounding triggers CDC-42 clustering following a burst of H₂O₂ in *C. elegans* epidermis
- CDC-42 clustering recruits WSP-1 to promote actin polymerization-based wound closure
- CDC-42 PBR and CAAX motif-mediated membrane attachment is required for its clustering
- H₂O₂ negatively regulates CDC-42 clustering through its Cys18 and Cys105 residues

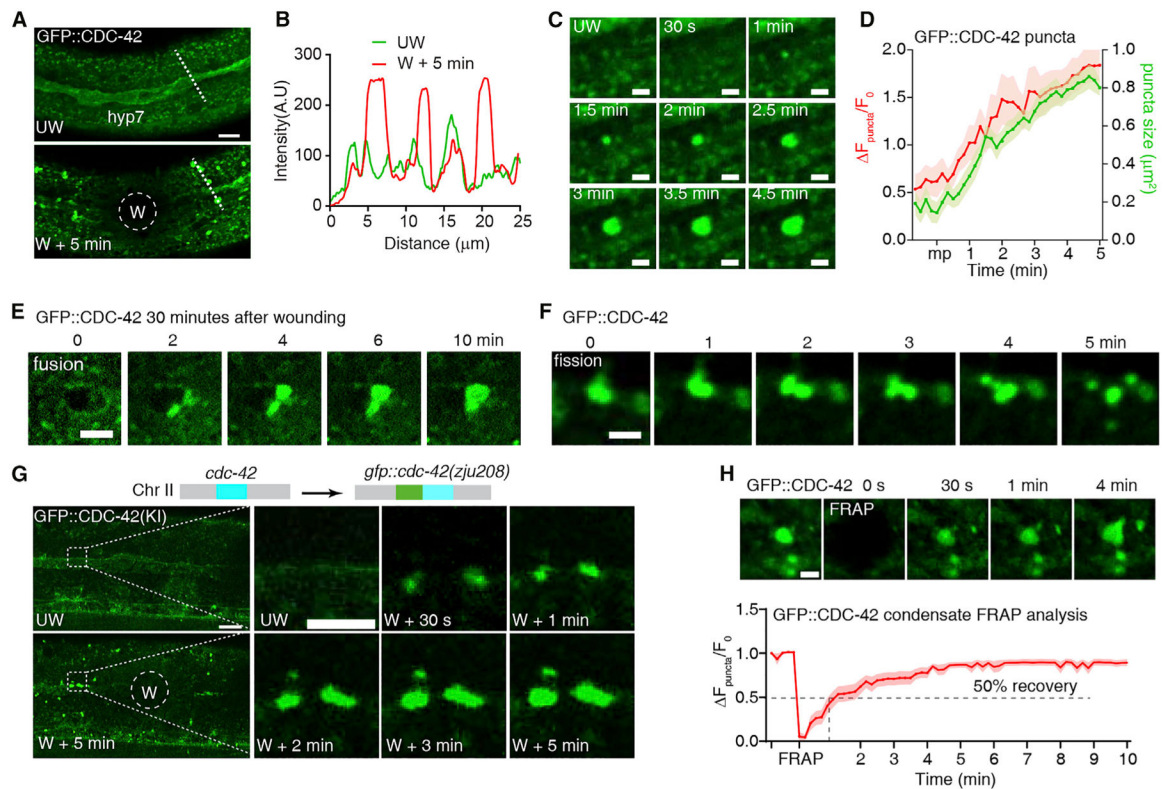


Figure 1. Wounding triggers rapid clustering of CDC-42 in *C. elegans* syncytial epidermis
 (A) Representative confocal images of GFP::CDC-42 with maximum intensity projection before and after laser wounding. Single-copy insertion of the *Pcol-19-GFP::CDC-42(zjuSi2)* transgenic animal was used for wounding and imaging. The white dashed circle indicates the wound site, and the white dashed lines indicate the analysis region. UW, unwounded; W, wounded.
 (B) Line scan analysis of GFP::CDC-42 fluorescence intensity in UW and W epidermis shown in (A).
 (C) Representative confocal images of single GFP::CDC-42 cluster growth at different time points after laser wounding.
 (D) Quantification of the size and fluorescence intensity of the GFP::CDC-42 clusters after wounding. n = 160 clusters.
 (E) Representative confocal images of GFP::CDC-42 clusters fusion after laser wounding.
 (F) Representative confocal images of GFP::CDC-42 clusters fission after laser wounding.
 (G) Top: schematic illustration of *GFP::cdc-42* knockin (KI) strategy by CRISPR-Cas9-mediated genome editing. Bottom: representative confocal images of endogenous GFP::CDC-42 cluster formation after laser wounding. *GFP::CDC-42(zju208)* KI animal was used for wounding and imaging.
 (H) Top: representative confocal images of GFP::CDC-42 cluster recovery at different time points after bleaching. *Pcol-19-GFP::CDC-42(zjuSi2)* transgenic animal was used for wounding and imaging. Bottom: quantification of the size and fluorescence intensity of the GFP::CDC-42 cluster recovered after FRAP. n = 16 animals.

Scale bars: 10 μm in (A) and (G); 5 μm in (G) of zoomed-in image; and 2 μm in (C), (E), (F), and (H). See also Figure S1 and Videos S1–S12 (see Mendeley data).

Author Manuscript

Author Manuscript

Author Manuscript

Author Manuscript

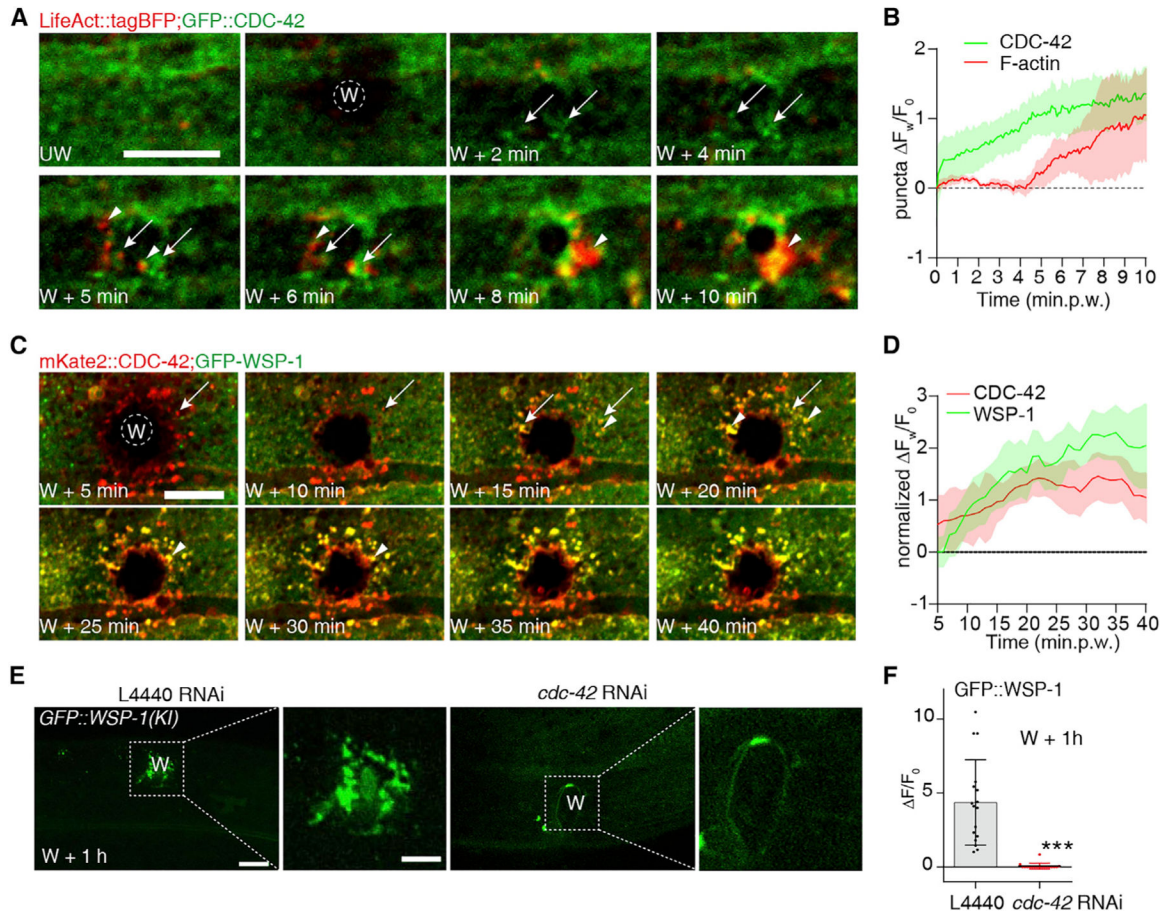


Figure 2. CDC-42 clustering recruits WSP-1 to promote actin polymerization-based wound closure

(A) Fluorescence confocal images of maximum projection of F-actin and CDC-42 around the wound site at different time points after laser wounding. White dashed circles indicate the wound site. Single-copy insertions of *Pcol-19-LifeAct::tagBFP(zjuSi83);Pcol-19-GFP::CDC-42(zjuSi2)* transgenic animal was used for wounding and imaging. White arrows indicate the GFP::CDC-42 puncta; LifeAct::tagBFP is shown in red.

(B) GFP::CDC-42 and LifeAct::tagBFP intensity change analysis after laser wounding. Note CDC-42 puncta formed ahead of F-actin polymerization. The plot indicates the mean \pm SEM at each time point. n = 10 animals.

(C) Representative confocal time-lapse images of CDC-42 and WSP-1 at the neighbor region to the wound site after needle wounding. White dashed lines indicate the analysis area. *Pcol-19-mKate2::CDC-42(zjuSi108);Pcol-19-GFP::WSP-1(zjuSi173)* animals were used for wounding and imaging. White arrows indicate the CDC-42 puncta; white arrowheads indicate the WSP-1 puncta formed at the CDC-42 puncta.

(D) Fluorescence intensity change analysis mKate2::CDC-42 and GFP::WSP-1 after needle wounding. The plot indicates the mean \pm SEM at each time point. n = 10 animals.

(E) Representative confocal images of GFP::WSP-1 at the wound site in L4440 and *cdc-42* RNAi-treated animals. *GFP::WSP-1 (cas723)(KI)* animal was used for wounding and imaging.

(F) Quantification of GFP::WSP-1 fluorescence signal in the animals with L4440 and *cdc-42* RNAi 1 h after wounding. Bars indicate mean \pm SD; L4440, n = 17; *cdc-42*, n = 18. ***p < 0.001, Mann-Whitney test.

Scale bars: 10 μ m in (A), (C), and (E) and 5 μ m in (E) of zoomed-in image. See also Figure S2 and Videos S13–S19 (see Mendeley data).

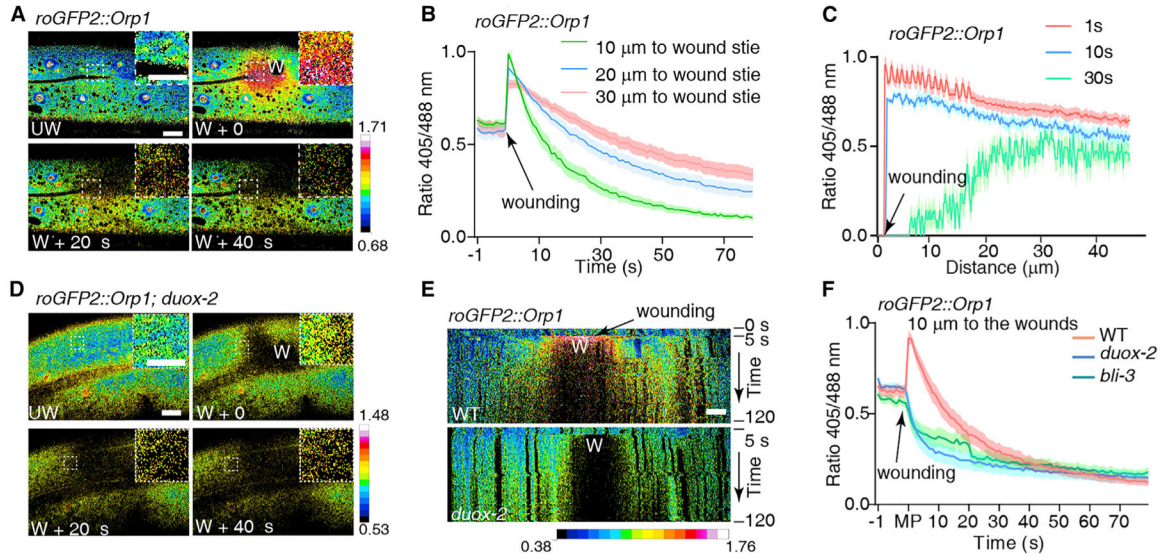


Figure 3. Wounding induced a local burst and reduction of H₂O₂ in the syncytia epidermis
 (A) Representative confocal ratiometric images of roGFP2::Orp1 in epidermal cells before and at different time points after wounding. *Pcol-19-roGF-P2::Orp1(zjuSi16)* single-copy transgenic animals were used for wounding and imaging. White W indicates the wound site. Dashed squares indicate the zoomed-in area.
 (B) Quantification of the roGFP2::Orp1 405/488 nm ratio at 10, 20, and 30 μm from the wound site over a time-lapse course. The plot shows the mean ratio of samples from 14 animals.
 (C) Quantification of the roGFP2::Orp1 405/488 nm ratio at different time points from the wound site to the neighboring region. The plot shows the mean ratio of samples from 15 animals.
 (D) Representative confocal ratiometric images of roGFP2::Orp1 before and different time points after wounding in *duox-2(ok1775)* mutant. *duox-2(ok1775); Pcol-19-roGFP2::Orp1(zjuSi16)* animals were used for wounding and imaging. White squares indicate the zoomed-in area.
 (E) Kymograph analysis of the roGFP2::Orp1 ratiometric (405/488 nm) signals at the wound area in the WT and *duox-2(ok1775)* mutant. Laser wounding was performed at 5 s in the images. Images are shown in pseudocolor (A and D).
 (F) Quantification of the roGFP2::Orp1 fluorescent ratio at 10 μm at the wound site with a time lapse in the WT, *duox-2(ok1775)*, and *bli-3(e767)* animals. The plot shows the mean ratio from 15 animals.
 Scale bars: 10 μm in (A), (D), and (E) and 5 μm in (A) and (D) of zoomed-in images. See also Figure S3 and Videos S20–S22 (see Mendeley data).

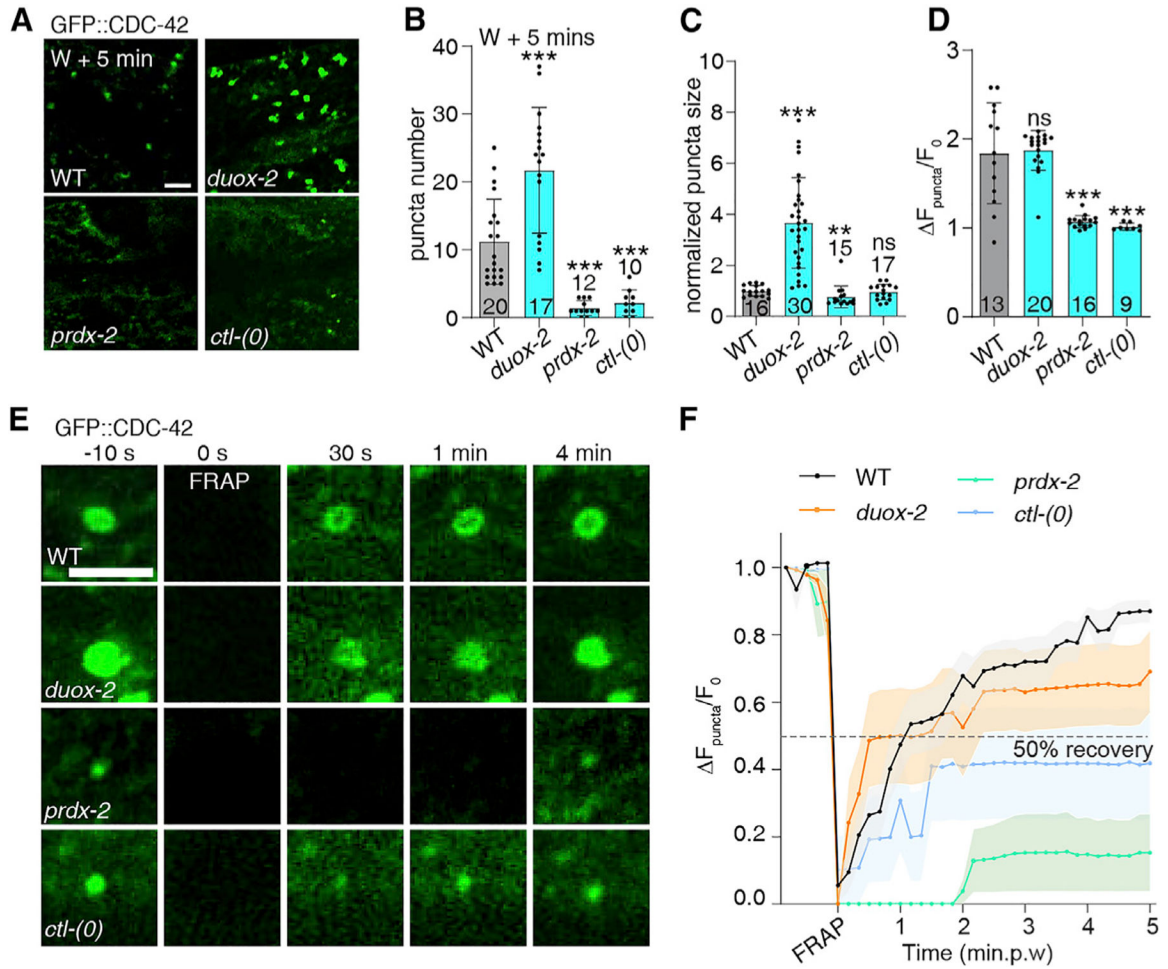


Figure 4. Reduction of H₂O₂ enhances wounding-induced CDC-42 clustering

(A) Representative confocal images of GFP::CDC-42 clusters in the epidermal cells in WT, *duox-2(ok1775)*, *prdx-2(gk169)*, and *ctl-1,2,3(zju181)* mutant animals 5 min after laser wounding. *Pcol-19-GFP::CDC-42(zjuSi2)* transgenic animals were in the background. *ctl-(0)* indicates the *ctl-1,2,3(zju181)* deletion allele.

(B) Quantification of the number of GFP::CDC-42 clusters in epidermal cell 5 min after laser wounding shown in (A). Bars indicate mean \pm SD; n values are listed in each bar. ***p < 0.001 compared with WT, one-way ANOVA.

(C) Quantification of the size of the GFP::CDC-42 cluster 5 min after laser wounding shown in (A). Bars indicate mean \pm SD; n values are listed in each bar. ***p < 0.001 compared with WT, one-way ANOVA. Puncta size was normalized to the WT.

(D) Quantification of the fluorescence intensity of the GFP::CDC-42 clusters in epidermal cell 5 min after laser wounding shown in (A). Bars indicate mean \pm SD; n values are listed in each bar. ***p < 0.001 compared with WT, one-way ANOVA. Animals not displaying puncta are not included in the statistics (16.7% in *prdx-2[gk169]* and 20% in *ctl-1,2,3[zju181]*).

(E) Representative confocal images of the GFP::CDC-42 clusters after photobleaching in the WT, *duox-2(ok1775)*, *prdx-2(gk169)*, and *ctl-1,2,3(zju181)* mutant animals.

(F) Quantification of the fluorescent change of the GFP::CDC-42 cluster recovery after photobleaching in the animals shown in (E). Bars indicate mean \pm SEM; n = 16 (WT), n = 10 (*duox-2*), n = 10 (*prdx-2*), and n = 10 (*ctl-0*) animals.

Scale bars: 5 μ m in (A) and (E). See also Figure S4 and Videos S23–S25 (see Mendeley data).

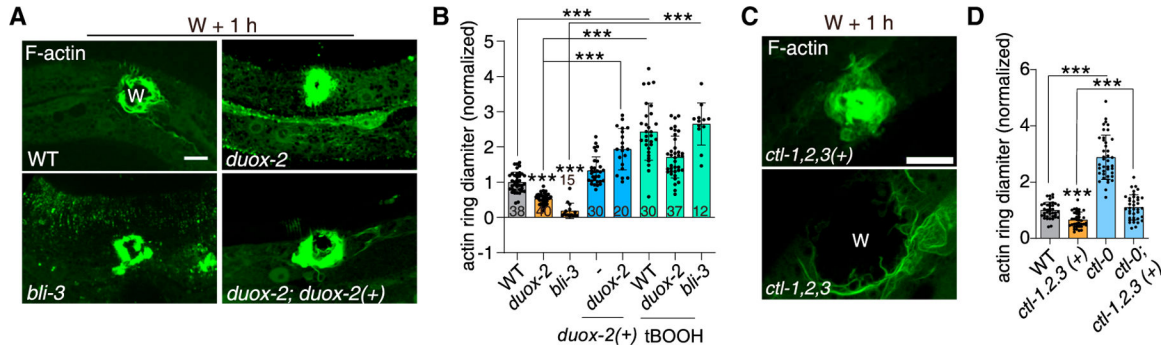


Figure 5. Reduction of H₂O₂ promotes actin polymerization-based wound closure
 (A) Representative confocal images of actin ring formation in WT, *duox-2(ok1775)*, *bli-3(e767)*, and *duox-2(ok1775);Pduox-2-duox-2(zjuEx703)* animals 1 h post-wounding (1 h.p.w.). *Pcol-19-GFP::moesin(zjuSi38)* transgenic animal was used to label F-actin.
 (B) Quantification of actin ring diameter 1 h.p.w. Bars indicate mean ± SD; n values are listed in each bar. tBOOH: 1 mM. ***p < 0.001 compared with WT, one-way ANOVA.
 (C) Representative confocal images of actin ring formation 1 h.p.w in *ctl-0* mutant and catalase overexpression strains *ctl-1,2,3(wuIs151+)*.
 (D) Quantification of actin ring diameter in WT, *ctl-1,2,3(wuIs151+)*, *ctl-0*, and *ctl-0;ctl-1,2,3(wuIs151+)* animals 1 h.p.w. *Pcol-19-GFP::moesin(juIs352)* transgene was in the background. Bars indicate mean ± SD; n values are listed in each bar. ***p < 0.001 compared with WT, one-way ANOVA.
 Scale bars: 10 μm in (A) and (C). See also Figure S5 and Video S26 (with the Mendeley dataset: 10.17632/zy2gmmcxp8.1).

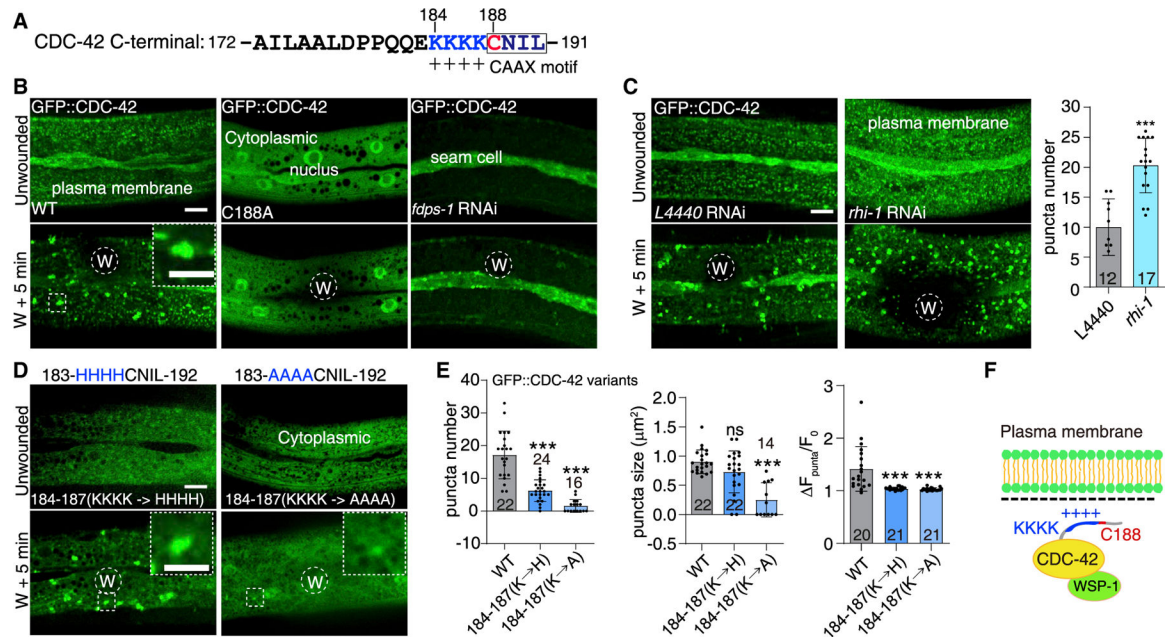


Figure 6. Membrane attachment is required for rapid CDC-42 clustering upon wounding
 (A) Illustration of the CDC-42 C-terminal protein sequence. Blue KKKK is the highly positively charged polybasic region (PBR), and CNIL is the CAAX motif.
 (B) Representative confocal images of GFP::CDC-42 in WT, C188A mutant, and *fdps-1* RNAi animals before and 5 min after wounding. *Pcol-19-GFP::CDC-42(C188A)(zjuEx975)* transgenic animal was used for C188A mutation, which blocked the prenylation and membrane attachment.
 (C) Left: representative confocal images of GFP::CDC-42 in *rhi-1* and control RNAi-treated animals before and 5 min after wounding. Right: quantification of the number of GFP::CDC-42 clusters in *rhi-1* and control RNAi animals. Bars indicate mean \pm SD; n values are listed in each bar. *** $p < 0.001$ compared with L4440 RNAi, Mann-Whitney test.
 (D) Representative confocal images of GFP::CDC-42 in *Pcol-19-GFP::CDC-42(KKKK \rightarrow HHHH)(zjuEx1004)* and *Pcol-19-GFP::CDC-42(KKKK \rightarrow AAAA)(zjuEx1002)* transgenic animals before and 5 min after wounding.
 (E) Quantification of the number, intensity, and size of GFP::CDC-42 clusters in each CDC-42 variant 5 min after wounding shown in (D). Bars indicate mean \pm SD; n values are listed in each bar. *** $p < 0.001$ compared with WT, one-way ANOVA.
 (F) Illustration of a proposed model of CDC-42 membrane attachment by Cys188 and PBR. Cys188-mediated prenylation and PBR are required for membrane attachment and wounding-induced CDC-42 clustering.
 Scale bars: 10 μ m in (B)–(D) and 5 μ m in (B) and (D) of zoomed-in images. See also Figure S6 and Videos S27–S30 (see Mendeley data).

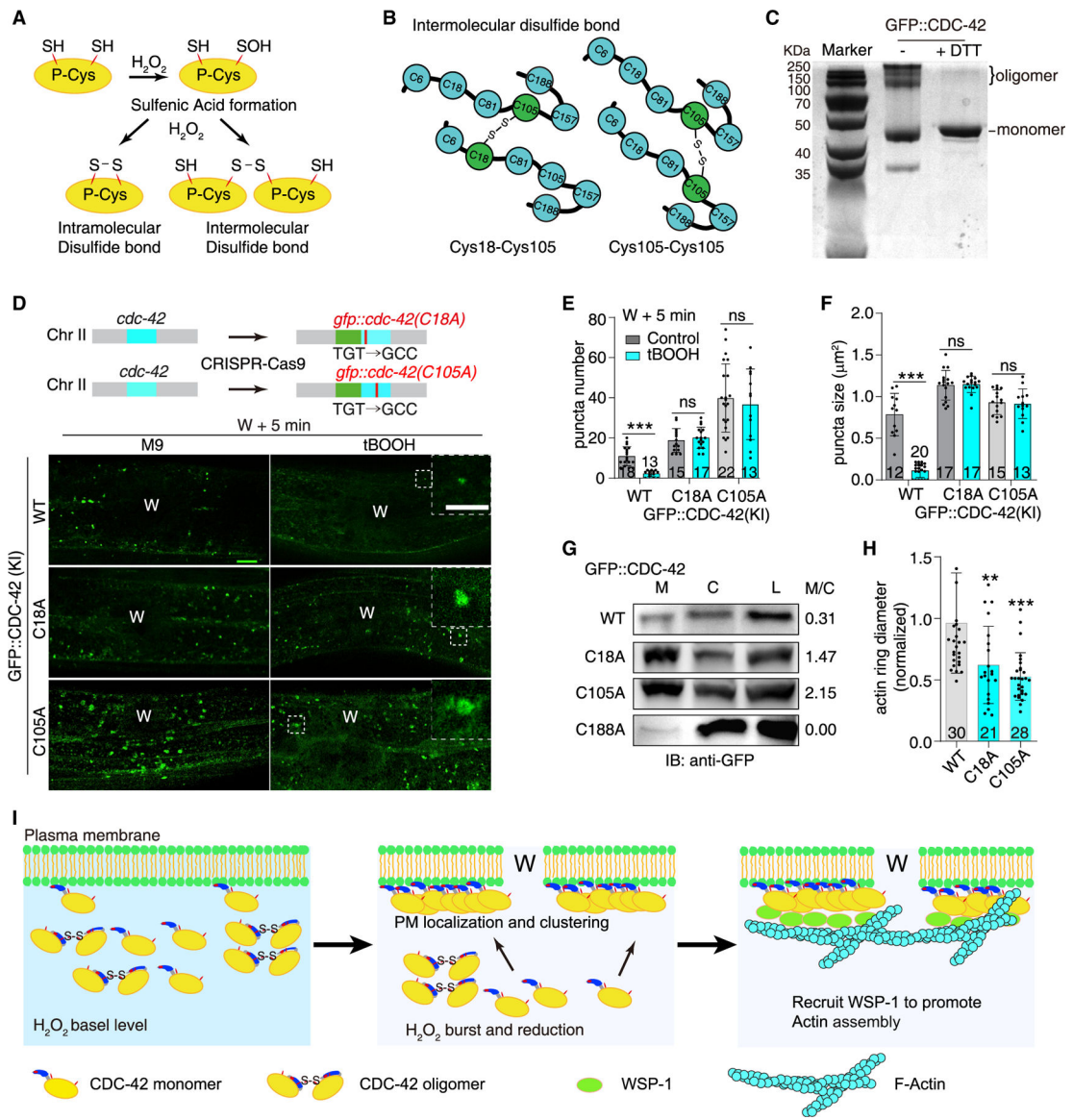


Figure 7. CDC-42 Cys18 and Cys105 are required for its sensing to H₂O₂ and clustering

(A) Illustration of potential disulfide bond formation by H₂O₂-mediated cysteine oxidation.

(B) Mass spectrometry analysis of CDC-42 indicates the intermolecular disulfide bond formation between Cys18-Cys105 and Cys105-Cys105.

(C) SDS-PAGE gel analysis of worm GFP::CDC-42 protein purified from the 293T cells with and without reduction. Dithiothreitol (DTT) was added to reduce the redox state and decrease the oligomerization of CDC-42.

(D) Top: diagram of the CRISPR-Cas9-mediated knockin strategy for *GFP::CDC-42^{C18A}* (*zju210*) and *GFP::CDC-42^{C105A}* (*zju223*) animals.

Bottom: representative images of endogenous *GFP::CDC-42^{WT}* (*zju208*),

GFP::CDC-42^{C18A} (*zju210*), and *GFP::CDC-42^{C105A}* (*zju223*) clusters before and 5 min after wounding with or without tBOOH (1 mM) treatment.

- (E) Quantification of the numbers of GFP::CDC-42 clusters before and 5 min after wounding in the *GFP::CDC-42^{WT}*(zju208), *GFP::CDC-42^{C18A}*(zju210), and *GFP::CDC-42^{C105A}*(zju223) mutant animals shown in (D). Bars indicate mean \pm SD; n values are listed in each bar. ***p < 0.001 compared with WT, one-way ANOVA.
- (F) Quantification of the size of the GFP::CDC-42 clusters before and 5 min after wounding in WT, C18A, and C105A mutant animals shown in (E). Bars indicate mean \pm SD; n values are listed in each bar. ***p < 0.001 compared with WT, one-way ANOVA.
- (G) Western blot to detect GFP::CDC-42 after subcellular fraction using whole animals. Pcol-19-GFP::CDC-42^{WT}(zjuSi2), Pcol-19-GFP::CDC-42^{C18A}(zjuSi138), Pcol-19-GFP::CDC-42^{C105A}(zjuSi190), and Pcol-19-GFP::CDC-42^{C188A}(zjuEx975) animals were used for cellular fraction. About 1,000 animals of each knockin or transgenic were used for each experiment. Results are from three replicated experiments. M, membrane; C, cytosolic; L, total lysate; M/C, GFP::CDC-42 ratio in membrane and cytosol.
- (H) Quantification of the actin ring diameter in *GFP::cdc-42^{WT}*(zju208), *GFP::cdc-42^{C18A}*(zju210), and *GFP::cdc-42^{C105A}*(zju223) animals shown in (F). Bars indicate mean \pm SD; n values are listed in each bar. ***p < 0.001 compared with WT, one-way ANOVA.
- (I) Diagram of the potential mechanism of wounding-induced CDC-42 clustering in regulating epidermal wound repair in *C. elegans*. Epidermal wounding induces a local transient burst and immediate reduction of H₂O₂, which regulates CDC-42 clustering to recruit WSP-1 and promote actin polymerization-based wound closure. Scale bars: 10 μ m in (D) and 5 μ m in (D) of zoomed-in image. See also Figure S7 and Videos S31 and S32 (see Mendeley data).

KEY RESOURCES TABLE

REAGENT or RESOURCE	SOURCE	IDENTIFIER
Antibodies		
Cdc42 Recombinant Rabbit Monoclonal Antibody	Invitrogen	Cat#MA5-32472; RRID: AB_2809749
Rabbit Polyclonal anti-GFP	MBL	Cat#598; RRID: RRID: AB_591819
Goat Anti-Rabbit IgG, HRP	MULTI SCIENCES	Cat#GAR007;RRID: AB_2827833
Bacterial strains		
OP50	CGC	N/A
HT115	CGC	N/A
DH5 α	Tsingke	Cat#TSV-A07
DB3.1	WEIDI	Cat#DL1040
Chemicals, peptides, and recombinant proteins		
Anti-GFP agarose nanobeads	AlpaLife	Cat#KTSM1301
Protease Inhibitor Cocktail	Bimake	Cat#B14002
InStab™ Protease Inhibitor Cocktail	Bimake	20124ES03; CAS: 9087-70-1
Phenylmethanesulfonyl fluoride (PMSF)	YEASEN	20104ES03; CAS: 329-98-6
Diphenyleneiodonium chloride (DPI)	Sigma	D2926; CAS: 4673-26-1
3-Methyl-1-phenyl-2-pyrazoline-5-one (MCI-186)	Sigma-Aldrich	M70800; CAS: 89-25-8
tertiary-butylhydroperoxide (tBOOH) solution	Sigma-Aldrich	458139; CAS: 75-91-2
Critical commercial assays		
2X Phanta Max Master Mix	Vazyme	P515-AA
I-5 2X High-Fidelity Master Mix	MCLAB	Cat#I5HM-200
ClonExpress II One Step Cloning Kit	Vazyme	C112-02
ClonExpress MultiS One Step Cloning Kit	Vazyme	C113-02
Gateway LR clonase II	Invitrogen	Cat#11791-020
10X KLD Enzyme Mix	NEB	Cat#M0554S
T4 DNA Ligase	NEB	Cat#M0202L
BseR I	NEB	Cat#R0581S
Deposited data		
MS Proteomics Data	This paper	ProteomeXchange: PASS01707
Supplementary Videos	This paper	Mendeley Data: https://doi.org/10.17632/zy2gmmcxp8.1
Experimental models: Cell lines		
Human: 293T	National Collection of Authenticated Cell Cultures	GNHu17
Experimental models: Organisms/strains		
<i>C. elegans</i> N2 Bristol	CGC	N2
<i>duox-2 (ok1775)</i> (outcross) I	CGC	RB1505
<i>Pcol-19-GFP::moesin (juls352) I</i>	Xu and Chisholm, 2011	CZ14748

REAGENT or RESOURCE	SOURCE	IDENTIFIER
<i>Pcol-19-GFP::CDC-42 (zjuSi2) I</i>	This paper	SHX9
<i>Pcol-19-GFP::CDC-42 (C18A) (zjuSi138) I</i>	This paper	SHX1886
<i>Pcol-19-GFP::CDC-42 (C105A) (zjuSi190) I</i>	This paper	SHX2150
<i>Pcol-19-roGFP2::Orp1 (zjuSi16) IV</i>	This paper	SHX175
<i>GFP::cdc-42 (zju208) II</i>	This paper	SHX1438
<i>GFP::cdc-42 (C18A) (zju210) II</i>	This paper	SHX1623
<i>GFP::cdc-42 (C105A) (zju223) II</i>	This paper	SHX2166
See Table S1 for a complete list of strains	This paper	N/A
Oligonucleotides		
pCFJ210 For tagaaagtataggaacttcgtgtaaaacgacggccagt	pSX681	ZJU143
pCFJ210 Rev tcaaagaaatgccgacttacacaggaacagctatgacctg	pSX681	ZJU144
<i>cdc-42</i> sgRNA #1 caggtcacagtaatgatcgg	pSX1484	ZJU2409
<i>cdc-42</i> sgRNA #2 gtcgttgagatggagctgt	pSX1485	ZJU2411
<i>ctl-0</i> sgRNA #1 cattggatgtggtgagcagg	pSX799	ZJU399
<i>ctl-0</i> sgRNA #2 tgtagtttgcctcaaggcgg	pSX801	ZJU401
<i>roGFP-orp1 rev</i> atggcgatctgatgacagcgtattccacctttcaaaagtcttcg	pSX703	ZJU184
<i>roGFP-orp1</i> for ggacccttgagggtacagatggtgagcaaggcgag	pSX703	ZJU185
pdd9577 backbone for gtccaattactctcaacatccc	pSX1480	ZJU340
pdd9577 backbone rev accggtaccctcaaggctc	pSX1480	ZJU341
See Table S2 for a complete list of oligos	This paper	N/A
Recombinant DNA		
pCFJ210-hygR- <i>Pcol-19-GFP::CDC-42</i>	N/A	pSX518
GFP-CDC-42 KI repair template	This paper	pSX1480
GFP::cdc-42 repair template C18A	This paper	pSX1564
<i>Pcol-19-GFP::CDC-42 (C188A)</i>	This paper	pSX1884
<i>Pcol-19-GFP::CDC-42 (184–187 KKKK→AAAA)</i>	This paper	pSX1907
<i>GFP::cdc-42</i> repair template C105A	This paper	pSX1909
<i>Pcol-19-GFP::CDC-42 (C20 residues)</i>	This paper	pSX1911
pCFJ201-SEC- <i>Pcol-19-GFP::CDC-42 (C20 residues)</i>	This paper	pSX2042
<i>Pcol-19-GFP::CDC-42 (CNIL)</i>	This paper	pSX2296
<i>Pcol-19-GFP::CDC-42 (184–187, KKKK→HHHH)</i>	This paper	pSX2299
See Table S3 for a complete list of plasmids	This paper	N/A
Software and algorithms		
<i>ImageJ</i>	National Institutes of Health	https://imagej.nih.gov/ij/